OPEN ACCESS
IOP Publishing
Superconductor Science and Technology
Supercond. Sci. Technol. **38** (2025) 075008 (17pp)
https://doi.org/10.1088/1361-6668/ade0f2

Extending the kinetic-inductance travelling wave parametric amplifiers coupled-mode framework to other symmetric nonlinear mediums with $\chi^{(3)}$ nonlinearity

Javier Navarro Montilla* **and Boon-Kok Tan**

Department of Physics (Astrophysics), University of Oxford, Denys Wilkinson Building, Keble Road, OX1 3RH Oxford, United Kingdom

E-mail: javier.navarro-montilla@stfc.ac.uk

Received 22 April 2025, revised 26 May 2025
Accepted for publication 4 June 2025
Published 3 July 2025

Abstract

Superconducting travelling-wave parametric amplifiers (TWPAs) play a vital role in a range of high-sensitivity applications. These devices can be realised using various superconducting materials, such as high kinetic inductance films or low-loss transmission lines embedded with discrete nonlinear elements like Josephson junctions (JJs) or superconducting quantum interference devices (SQUIDs), and can operate across different wave-mixing regimes. However, a unifying framework for quick assessment and thus efficiently evaluating the performance of these diverse TWPA architectures, particularly during the design phase, remains lacking. Most existing models are derived from first principles for specific TWPA designs and lack general applicability. While certain simulation program with integrated circuit emphasis (SPICE) tools can more accurately emulate TWPA behaviour post-design, they are typically computationally intensive, time-consuming, and offer limited physical insight; especially regarding key performance-determining factors such as phase matching. This, in turn, impedes the rapid identification of optimal TWPA configurations. In this work, we extend a previously introduced framework for kinetic-inductance (KI-) TWPAs and demonstrate its applicability to a broader class of $\chi^{(3)}$-type TWPA configurations, including bare JJ (JTWPA) and symmetric SQUID-based TWPAs, operating in all wave-mixing modes. This approach facilitates rapid design-space exploration prior to detailed optimisation using SPICE-based simulations. Our method accommodates a wide range of unit cell topologies and meta-material parameters without requiring ground-up derivations from first principles. We validate the framework by

* Author to whom any correspondence should be addressed.

comparing it against representative models from the literature, including JJ-, KI-, and DC SQUID-based TWPA designs, and show that it reliably captures the first-order behaviour of their gain–bandwidth characteristics.

Keywords: travelling-wave, parametric amplifier, Josephson junctions, SQUID, kinetic inductance, coupled-mode equations

1. Introduction

Signal amplification is a fundamental requirement across a broad range of physical systems, from classical electronic circuits to quantum optical platforms. In the domain of superconducting devices, resonance-cavity-based superconducting parametric amplifiers, particularly Josephson-junction parametric amplifiers (JPAs), leverage the current-dependent nonlinear reactance of Josephson junctions (JJs), analogous to the Kerr effect in optics, to facilitate amplification via wave-mixing processes. JPAs have demonstrated performance approaching the quantum noise limit [1–4], and play a pivotal role in a wide array of ultra-sensitive experiments. These include rapid, high-fidelity quantum state readout [5], quantum non-demolition measurements [6–9], and the search for axion dark matter candidates [10–14]. However, JPAs are inherently narrowband, with typical bandwidths ranging from tens to hundreds of megahertz.

Superconducting travelling-wave parametric amplifiers (TWPAs) offer a compelling alternative by replacing the resonant cavity with a long, nonlinear transmission line [15, 16], enabling extended interaction between a weak signal and a strong pump without the bandwidth constraints imposed by the resonance-cavity. As a result, TWPAs can achieve gigahertz-scale amplification bandwidths while maintaining quantum-limited sensitivity [17, 18]. The required low-dissipation nonlinear medium can be realised using high kinetic inductance (KI) superconducting wires fabricated from materials such as titanium nitride (TiN) or niobium TiN (NbTiN) [19]. Alternatively, nonlinear media can be constructed using arrays of JJs [20–22] or superconducting quantum interference devices (SQUIDs) [23, 24] embedded in low-loss superconducting transmission lines (STLs).

Various TWPA architectures have been reported in the literature [19, 22–30], differentiated by their nonlinear media and wave-mixing regimes: including three-wave mixing (with or without DC bias current[1]), degenerate-pump four-wave mixing (DP4WM), and non-DP4WM (NP4WM). Despite this diversity, most theoretical models have been developed independently and tailored to specific designs [31–37]. While feasible, this approach becomes increasingly cumbersome for more complex geometries or when comparing architectures for specific applications.

In this manuscript, we extend a previously introduced framework developed for kinetic-inductance TWPAs (KITWPAs), and demonstrate that, as originally suggested by Eom *et al* [19], it can be generalised to accurately describe the behaviour of a broad class of $\chi^{(3)}$-type TWPAs. This includes devices based on JJs, symmetric DC SQUIDs, and high-KI films, across all wave-mixing regimes. Our framework incorporates several improvements over prior formulations: it eliminates the need for translational symmetry assumptions, accounts for temperature-dependent losses and material properties, and includes electromagnetic interactions between components within the amplifier chip. This allows the more detailed treatment of the phase-matching schemes, such as periodic impedance modulation [26, 28, 34, 38, 39] and resonant phase-matching techniques [25, 32], both of which are essential for achieving exponential gain.

While commercial simulation program with integrated circuit emphasis (SPICE)-based simulation tools such as WRspice or Keysight® advanced design system (ADS) can model subtle device-level effects and offer excellent agreement with experimental performance, particularly for JTWPA configurations, they provide limited physical insight and are typically resource-intensive. Our primary goal here is to accelerate the TWPA design process by offering a generalised, physics-informed framework that enables rapid design exploration across diverse architectures, prior to detailed optimisation via circuit-level simulation.

2. Extended coupled-mode equations (CME) framework

We begin with the general telegrapher's equations [40], which describe the propagation of current $I(z,t)$ along a transmission line as a function of time t and and spatial coordinate z:

$$\frac{\partial^2 I(z,t)}{\partial z^2} = RG\cdot I + (RC+LG)\frac{\partial I}{\partial t} + C\frac{\partial}{\partial t}L\frac{\partial I(z,t)}{\partial t}, \quad (1)$$

where R, L, G, C denote the per-unit-length resistance, inductance, conductance, and capacitance of the transmission line, respectively. This expression characterises the dynamics of a passive, linear transmission line.

To incorporate nonlinear effects relevant to TWPAs, we replace the reactive (inductive or capacitive) terms with their nonlinear counterparts, depending on the nature of the parametric medium employed. In this work, we focus on TWPAs where nonlinearity arises from a current-dependent inductance. Assuming $I \ll I_*$, we generalise the nonlinear

[1] The former arises from symmetry breaking in $\chi^{(3)}$ Kerr media via DC biasing, whereas the latter is intrinsic to $\chi^{(2)}$ media.

inductance of such STLs as[2]:

$$L(I) = L_0 \left[1 + \beta_{\rm nl} \left(\frac{I}{I_*}\right)^2\right], \tag{2}$$

where L_0 is the intrinsic (linear) inductance and I_* sets the scale of nonlinearity. Here, we introduce the constant $\beta_{\rm nl}$ which takes different values depending on the source of nonlinearity in the STL. In the following sections, we derive the appropriate expressions for $\beta_{\rm nl}$ corresponding to various nonlinear media used in TWPA implementations.

2.1. Derivation of nonlinear inductance terms

Kinetic inductance.— Early theoretical and experimental studies have demonstrated that superconductors exhibit a nonlinear current dependence in their electromagnetic response, particularly in the kinetic inductance. This nonlinearity can be described within the framework of the Kupriyanov-Lukichev-Maki formulation of current-carrying Bardeen–Cooper–Schrieffer (BCS) theory, which models the suppression of the superconducting order parameter due to supercurrent flow [41]. A widely used phenomenological expression for the current-dependent kinetic inductance is given by [42]:

$$L_k(I) = L_0 \left[1 + \frac{I^2}{I_*^2}\right], \tag{3}$$

where I_* is a characteristic current scale typically on the order of the depairing current. The validity of this expression has been supported by extensive experimental work, particularly in the development of superconducting resonators with high kinetic inductance [43]. While this model effectively captures the essential nonlinear behaviour, more rigorous derivations of the current-dependent kinetic inductance have been developed using nonequilibrium superconductivity formalisms such as the Keldysh–Eilenberger and Keldysh–Usadel approaches. These methods provide a more comprehensive microscopic foundation, accounting for effects such as impurity scattering and collective mode (Higgs mode) contributions [44–47]. Accordingly, within the scope of this approximation, the nonlinear coefficient is taken as $\beta_{\rm nl} = 1$.

JJ.— The current in a JJ is given by the first Josephson equation:

$$I = I_{\rm c} \sin\phi, \tag{4}$$

where $I_{\rm c}$ is the critical current and ϕ is Josephson phase across the junction. From the definition of the inductance $\left(v(t) = L\frac{{\rm d}i}{{\rm d}t}\right)$ and the Josephson equations, the inductance of a JJ can be written as:

$$L_j = \frac{\phi_0}{I_{\rm c}\cos\phi}, \tag{5}$$

where ϕ_0 is the reduced magnetic flux quantum. Given the trigonometry identity $\sin^2\phi + \cos^2\phi = 1$, we can rewrite $\cos\phi = \sqrt{1-\sin^2\phi} = \sqrt{1-\left(\frac{I}{I_{\rm c}}\right)^2}$. By replacing this expression in equation (5), we obtain:

$$L_{\rm j} = \frac{L_0}{\sqrt{1-\left(\frac{I}{I_{\rm c}}\right)^2}}, \tag{6}$$

where $L_0 = \frac{\phi_0}{I_{\rm c}}$. Assuming $I \ll I_{\rm c}$, we apply the Taylor expansion to the first order of the denominator in the above equation, resulting in the following expression of the junction's inductance:

$$L_{\rm j} = L_0 \left[1 + \frac{1}{2}\left(\frac{I}{I_{\rm c}}\right)^2\right]. \tag{7}$$

Therefore, the nonlinear constant $\beta_{\rm nl} = 0.5$.

DC-SQUID.— For symmetric DC-SQUID where both the junctions in parallel are identical, the total current in the DC-SQUID is given by [48]:

$$\begin{aligned} I_{\rm sq} &= I_{\rm j_1} + I_{\rm j_2} \\ &= I_{\rm c}\sin\phi_1 + I_{\rm c}\sin\phi_2 \\ &= 2I_{\rm c}\sin\left(\frac{\phi_1+\phi_2}{2}\right)\cos\left(\frac{\phi_1-\phi_2}{2}\right). \end{aligned} \tag{8}$$

Given the geometry of the DC-SQUID, when applying an external DC magnetic flux $\Phi_{\rm dc}$, it induces an opposite phase change $\phi_{\rm M}$ in each junction of the DC-SQUID i.e. $\phi_1 = \phi + \phi_{\rm M}$ and $\phi_2 = \phi - \phi_{\rm M}$ where ϕ is the Josephson phase of a single junction. Therefore,

$$\phi_1 - \phi_2 = 2\phi_{\rm M} = 2\pi\frac{\Phi_{\rm dc}}{\Phi_0}, \tag{9}$$

where Φ_0 is the magnetic flux quantum. Hence, we can rewrite the current in a DC-SQUID as:

$$I_{\rm sq} = 2I_{\rm c}\cos\left(\pi\frac{\Phi_{\rm dc}}{\Phi_0}\right)\sin\phi = I_{\rm c,sq}\sin\phi, \tag{10}$$

where $I_{\rm c,sq} = 2I_{\rm c}\cos\left(\pi\frac{\Phi_{\rm dc}}{\Phi_0}\right)$.

The inductance of the DC-SQUID is given by the equivalent inductance of both junctions in parallel:

$$\begin{aligned} L_{\rm sq} &= \frac{L_{\rm j_1}L_{\rm j_2}}{L_{\rm j_1}+L_{\rm j_2}} \\ &= \frac{\phi_0}{I_{\rm c}}\left[\frac{1}{\cos\phi_1+\cos\phi_2}\right] \\ &= \frac{\phi_0}{2I_{\rm c}\cos\left(\pi\frac{\Phi_{\rm dc}}{\Phi_0}\right)\cos\phi} \\ &= \frac{\phi_0}{I_{\rm c,sq}\cos\phi}. \end{aligned} \tag{11}$$

From equation (10), $\sin\phi = \frac{I_{\rm sq}}{I_{\rm c,sq}}$, hence using the same trigonometry identity used in the JJ case, we can rewrite $\cos\phi =$

[2] As introduced in Sec. IIA this expression is derived from a first-order Taylor expansion under the assumption that — a condition typically satisfied in standard TWPA operation. However, at higher currents approaching , the neglected higher-order terms may become significant, potentially altering the device behaviour by enabling stronger energy transfer to spurious frequency components and thereby degrading the signal gain.

Table 1. Nonlinear inductance parameters for the different sources of inductance in a TWPA. R_N denotes the normal resistance, Δ the superconducting gap and I_{dp} the depairing current of the superconductor. The coefficient α corresponds to $C^{-1/2}$ in [45].

	Kinetic inductance	Josephson junctions	DC-SQUID
β_{nl}	1	0.5	0.5
L_0	$\hbar R_N/\pi\Delta$	ϕ_0/I_*	ϕ_0/I_*
I_*	αI_{dp}	I_c	$2I_c\cos\left(\pi\frac{\Phi_{dc}}{\Phi_0}\right)$

$\sqrt{1-\left(\frac{I_{sq}}{I_{c,sq}}\right)^2}$. Assuming $I_{sq} \ll I_{c,\,sq}$, we apply the first-order Taylor expansion and replacing $\cos\phi$ in equation (11):

$$L_{sq} = L_{0,sq}\left[1+\frac{1}{2}\left(\frac{I_{sq}}{I_{c,sq}}\right)^2\right], \tag{12}$$

where $\beta_{nl} = 0.5$. In the case where there is no external DC magnetic flux ($\Phi_{dc} = 0$), $I_{c,sq} = 2I_c$ and $L_{0,sq} = \frac{\phi_0}{2I_c} = \frac{L_0}{2}$,

$$L_{sq} = \frac{L_0}{2}\left[1+\frac{1}{2}\left(\frac{I_{sq}}{2I_c}\right)^2\right], \tag{13}$$

where the total inductance is half of that of the case with a single JJ, and the nonlinearity term $(\frac{I}{I_*})^2$ is half the amplitude as well. The values for these parameters for various TWPA configurations are tabulated in table 1.

2.2. Extending CME equation

Combining the equations (1) and (2) with the corresponding β_{nl} value, we obtain the nonlinear transmission line equation:

$$\begin{aligned}\frac{\partial^2 I}{\partial z^2} - RG\cdot I(z,t) - (RC+L_0G)\frac{\partial I(z,t)}{\partial t} - L_0C\frac{\partial^2 I}{\partial t^2}\\ - \frac{\beta_{nl}L_0C}{I_*^2}\frac{\partial}{\partial t}\left(I^2\frac{\partial I}{\partial t}\right) - \frac{\beta_{nl}L_0G}{I_*^2}\left(I^2\frac{\partial I}{\partial t}\right) = 0,\end{aligned} \tag{14}$$

where the fifth and sixth terms are the mixing terms. This equation describes the wave propagation in a nonlinear STL assuming that the nonlinear inductance is much larger than the geometric inductance of the transmission line ($L_0 \gg L_{geo}$), a legitimate assumption for highly nonlinear inductive mediums. For the case of a transmission line embedded with series of JJs, the large L_0 required for J- or DC-SQUID TWPAs results in a thicker junction insulator layer, which reduces the junction capacitance (C_j) substantially. In this scenario, L_0 dominates the total impedance of the junction and the contribution of the C_j is negligible (see appendix A for details). We acknowledge that the current model is limited to describing symmetric $\chi^{(3)}$ nonlinear media. In future work, we aim to extend the framework to include non-symmetric $\chi^{(2)}$ and $\chi^{(3)}$ nonlinear media, such as those employing RF-SQUIDs, superconducting nonlinear asymmetric inductive elements (SNAILs), or superconducting low-inductance undulatory galvanometers (SLUGs)-based nonlinear inductor.

The remaining derivation is largely similar to the CMEs formulated for the KITWPA, as described in [19], except that we further include the effects of conductance, shunted capacitance, and the attenuation constant [49]. This inclusion accounts for transmission line losses, which can have a non-negligible impact on TWPA performance [22, 23]. Assuming that the solutions are forward-propagating waves in the form

$$I(z,t) = \sum_m \frac{1}{2}A_m(z)\,e^{i\omega_m t-\gamma_m z} + \text{c.c.}, \tag{15}$$

and operation in the full NP4WM regime (the most generalised case) where $m = p_1, p_2, s, i$ denotes the two pump tones at different frequencies (p_1 and p_2), a signal (s) and an idler (i) tone, A_m the slowly varying amplitude of the waves, $\gamma_m = \alpha_m + i\beta_m = \sqrt{(R+i\omega_m L)(G+i\omega_m C)}$ the complex propagation constant, α_m the attenuation constant, β_m the wave vector, and ω_m the angular frequency. Substituting these into the nonlinear wave equation (equation (14)), under the slowly varying envelope approximation and by separating out the terms that oscillate at the pumps, signal and idler frequencies, we obtain the following coupled equations

$$\begin{aligned}\gamma_{p_1}\frac{\partial A_{p_1}(z)}{\partial z} = \left(1+i\frac{G}{\omega_{p_1}C}\right)\frac{\beta_{nl}\beta_{p_1}^2}{8I_*^2}\Big[A_{p_1}\left(\eta_{p_{11}}A_{p_1}A_{p_1}^*e^{-2\alpha_{p_1}z} + 2\eta_{p_{22}}A_{p_2}A_{p_2}^*e^{-2\alpha_{p_2}z} + 2A_sA_s^*e^{-2\alpha_s z} + 2A_iA_i^*e^{-2\alpha_i z}\right)\\ + 2A_{p_2}^*A_sA_ie^{(2\alpha_{p_1}-\Delta_\alpha)z}e^{-i\Delta_\beta z}\Big]\end{aligned} \tag{16a}$$

$$\begin{aligned}\gamma_{p_2}\frac{\partial A_{p_2}(z)}{\partial z} = \left(1+i\frac{G}{\omega_{p_2}C}\right)\frac{\beta_{nl}\beta_{p_2}^2}{8I_*^2}\Big[A_{p_2}\left(2\eta_{p_{11}}A_{p_1}A_{p_1}^*e^{-2\alpha_{p_1}z} + \eta_{p_{22}}A_{p_2}A_{p_2}^*e^{-2\alpha_{p_2}z} + 2A_sA_s^*e^{-2\alpha_s z} + 2A_iA_i^*e^{-2\alpha_i z}\right)\\ + 2A_{p_1}^*A_sA_ie^{(2\alpha_{p_2}-\Delta_\alpha)z}e^{-i\Delta_\beta z}\Big]\end{aligned} \tag{16b}$$

$$\gamma_s \frac{\partial A_s(z)}{\partial z} = \left(1 + i\frac{G}{\omega_s C}\right)\frac{\beta_{nl}\beta_s^2}{8I_*^2}\left[A_s\left(2A_{p_1}A_{p_1}^* e^{-2\alpha_{p_1}z} + 2A_{p_2}A_{p_2}^* e^{-2\alpha_{p_2}z} + A_s A_s^* e^{-2\alpha_s z} + 2A_i A_i^* e^{-2\alpha_i z}\right) + 2A_{p_1}A_{p_2}A_i^* e^{(2\alpha_s - \Delta_\alpha)z} e^{-i\Delta_\beta z}\right] \tag{16c}$$

$$\gamma_i \frac{\partial A_i(z)}{\partial z} = \left(1 + i\frac{G}{\omega_i C}\right)\frac{\beta_{nl}\beta_i^2}{8I_*^2}\left[A_i\left(2A_{p_1}A_{p_1}^* e^{-2\alpha_{p_1}z} + 2A_{p_2}A_{p_2}^* e^{-2\alpha_{p_2}z} + 2A_s A_s^* e^{-2\alpha_s z} + A_i A_i^* e^{-2\alpha_i z}\right) + 2A_{p_1}A_{p_2}A_s^* e^{(2\alpha_i - \Delta_\alpha)z} e^{-i\Delta_\beta z}\right], \tag{16d}$$

where $\Delta_\beta = \beta_{p_1} + \beta_{p_2} - \beta_s - \beta_i$ and $\Delta_\alpha = \alpha_{p_1} + \alpha_{p_2} + \alpha_s + \alpha_i$. Here, we introduce two coefficients $\eta_{p_{11}}$ and $\eta_{p_{22}}$ to generalise the set of equations for different regimes such as 3WM, DP4WM and NP4WM operation etc. More details on how to reduce the NP4WM mode into the DC-biased 3WM and DP4WM mode, and hence the numerical values of $\eta_{p_1 1}$ and $\eta_{p_{22}}$, can be found in appendix B. In this most general NP4WM case, $\eta_{p_{11}} = 1$ and $\eta_{p_{22}} = 1$.

This set of equations can be solved numerically to obtain the TWPA gain profile including the pump depletion effect. To obtain the analytical solution, we follow the same procedure as shown in [32]. We first assume an ultra low-loss STL where the terms $\frac{G}{\omega_m C}$ can be omitted[3], and the TWPA's operation in the undepleted pumps regime ($A_{p_1}, A_{p_2} \gg A_s \,\&\, A_i$). This results in a simplified set of CMEs (see appendix C for full derivation):

$$\frac{\partial a_s(z)}{\partial z} - i\kappa_s a_i^*(z) e^{i\Delta_\phi z} = 0 \tag{17a}$$

$$\frac{\partial a_i(z)}{\partial z} - i\kappa_i a_s^*(z) e^{i\Delta_\phi z} = 0, \tag{17b}$$

where the solution for the pump tones are $A_{p_1(z)} = A_{0,p_1} e^{i\varphi_{p_1} z}$ and $A_{p_2(z)} = A_{0,p_2} e^{i\varphi_{p_2} z}$ ($A_s(z) = a_s(z)e^{i\varphi_s z}$ and $A_i(z) = a_i(z)e^{i\varphi_i z}$ for the signal and idler respectively), with the required coefficients tabulated in table 5 for all the wave-mixing regimes. Following [50], we arrive at the solutions for the signal and idler:

$$a_s(z) = \left\{\left[\cosh(gz) - \frac{i\Delta_\phi}{2g}\sinh(gz)\right]a_s(0) + \left[\frac{i\kappa_s}{g}\sinh(gz)\right]a_i(0)\right\} e^{i\Delta_\phi z/2} \tag{18a}$$

$$a_i(z) = \left\{\left[\cosh(gz) - \frac{i\Delta_\phi}{2g}\sinh(gz)\right]a_i(0) + \left[\frac{i\kappa_s}{g}\sinh(gz)\right]a_s(0)\right\} e^{i\Delta_\phi z/2}, \tag{18b}$$

where $g = \sqrt{\kappa_s\kappa_i - \frac{\Delta_\phi^2}{4}}$ is the gain coefficient.

[3] The conductance G represents dielectric losses to the substrate in a TWPA. For typical design parameters — capacitance in the range $10\,\text{fF} < C < 100\,\text{fF}$ and operating frequencies $0.5\,\text{GHz} < \omega_m < 40\,\text{GHz}$—the factor $\left(1 + i\frac{G}{\omega_m C}\right)$ approximates unity if $G \ll \omega_m C$. This condition is met when $G \ll 10^{-5}\Omega$ which motivates the use of high-resistivity substrates, such as intrinsic silicon ($> 20\text{k}\Omega \cdot \text{cm}$), sapphire, or silica.

In contrast to most CME reported for $\chi^{(3)}$ nonlinear materials, as described earlier, we extend these expressions to account for all wave-mixing schemes, namely DC3WM, DP4WM, and NP4WM. This is achieved by introducing two additional coefficients, $\eta_{p_{11}}$ and $\eta_{p_{22}}$. With these additions, our framework can describe up to nine symmetric TWPAs with Kerr-3 ($\chi^{(3)}$) nonlinearity using the same set of equations, requiring only a few numerical coefficients. Table 5 in the appendix summarises the technical differences in defining these coefficients across different operating regimes and nonlinear inductive media. This table is intended to help readers replicate the calculations. By simply substituting these coefficients into the framework, users can simulate the gain-bandwidth product of these TWPAs with minimal modifications.

Furthermore, the expression of the pumps, signal and idler amplitudes in the framework only depends on three parameters: the propagation constant γ_m of the transmission line, and the two pump amplitudes ($I_{p_1} = |A_{p_1}|^2$ & $I_{p_2} = |A_{p_2}|^2$) over I_* for NP4WM example given here. For DP4WM case, only I_p/I_* is required; whereas for DC3WM mode, the DC current I_{dc} and the pump $I_p = |A_p|^2$. While the pumps/DC amplitudes are user-determined, the propagation constant is intrinsic to the TWPA design, and can be obtained using different techniques e.g. from circuit theory, from measured data or using electromagnetic (em) softwares like Ansys® High Frequency Structure Simulator (HFSS [51]) or Sonnet® [52]. Note that, in this formulation, the only parameter required to describe the nonlinear transmission line i.e. the TWPA itself, is indeed only the propagation constant γ_m. This approach therefore opens up the possibility to emulate many variance of TWPA designs using a variety of softwares and methods, and simply importing the propagation constant to the CME-framework to predict the gain-bandwidth product, without the need to built the theoretical model from first-principle for different circuit designs.

2.3. Obtaining dispersion relation

This final aspect—using electromagnetic simulators or alternative techniques to extract the required propagation constant γ_m — has been detailed for the case of KITWPAs in [49]. For completeness, we briefly summarise the methodology used to obtain the dispersion relation, extending it for TWPAs made with JJs. For a more comprehensive discussion, we refer the reader to [49].

From the framework described above, it is evident that the only unknown in the CME model pertaining to the STL is the frequency-dependent complex propagation constant, γ_m. This parameter encapsulates all the essential information required to describe the evolution of various frequency components (tones) as they propagate along the line. The propagation constant γ_m can be derived theoretically using a reduced Kirchhoff-equivalent circuit of a unit cell, typically represented in the form of `ABCD` matrices [34, 39], or by employing an `RLGC` model [36, 53] incorporating the complex surface impedance of superconducting materials and/or the nonlinear inductance of the junctions. The overall behaviour of the TWPA is then modelled by assuming translational symmetry of the structure, in accordance with the Floquet theorem, through the repetition of identical unit cells to form the full-length STL.

This simplified approach neglects many subtle effects that can emerge when cascading hundreds of unit cells and is therefore limited to relatively simple transmission line geometries. For instance, accurately modelling practical transmission lines such as coplanar waveguides (CPWs) with capacitive stubs or inverted microstrip becomes significantly more complex. Moreover, the calculation process is often lengthy and requires a number of specific assumptions tailored to the materials and geometries involved.

To circumvent these limitations, we leverage the versatility of commercial circuit simulators such as the 3D electromagnetic em software packages Ansys High Frequency Structure Simulator® (HFSS), the 2.5D Sonnet® package, or keysight ADS, to model the full physical layout of the unit cell. This approach offers significant flexibility in extracting the propagation constant γ_m, which can then be used within the framework described above to calculate the gain-bandwidth product of the complete TWPA. By working within these simulation environments, a wide range of structural complexities and design features can be readily incorporated into the analysis.

In the case of HFSS, accurately modelling the behaviour of the metal film in its superconducting state is essential. This is especially important for KITWPAs, where thin superconducting films are used. To achieve this within the electromagnetic model, we first calculate the film's complex surface impedance using the Mattis–Bardeen (MB) formalism [54]. This calculation incorporates key material parameters such as the film thickness, critical temperature (T_c), superconducting energy gap (V_{gap}), normal-state resistivity (ρ_N), and the operating bath temperature (T_{bath}). The resulting frequency-dependent complex surface impedance is then applied as an impedance boundary condition to a perfect electric conductor (PEC), effectively modelling the superconducting film.

It is important to note that the MB formalism assumes the superconductor is in thermal equilibrium and that the applied AC fields are sufficiently weak so as not to disturb the quasiparticle distribution or the superconducting gap. In the context of TWPAs, this assumption is typically valid, since proper amplifier operation requires currents well below the nonlinearity threshold, i.e. $I \ll I_*$, where I_* is on the order of the depairing current I_{dp} in KITWPAs. For JTWPAs, which employ relatively thick BCS superconducting films, the nonlinear kinetic inductance contribution is even further suppressed, and the induced current densities remain within the linear-response regime where MB theory is known to be accurate. However, under strong AC drive or significant DC bias, nonequilibrium effects can become relevant, requiring more sophisticated treatments beyond MB, such as those based on the Keldysh or Usadel formalisms [55, 56].

The *em* model is further refined by including the characteristics of the substrate and dielectric materials such as finite substrate resistivity and dielectric loss tangent as well as incorporating a realistic TWPA layout. This allows the inclusion of subtle electromagnetic effects such as fringing fields, radiative losses, discontinuities, and the geometric inductance and capacitance of the transmission line. In the JTWPA case, the junctions can be simulated by connecting to the transmission line structures with a lumped-*RLC* boundary condition with the capacitance and inductance value of the junction. Once the unit cell—comprising the main transmission line and further structures for dispersion engineering e.g. impedance loading sections or *LC* resonators—is fully defined, we extract its `ABCD` matrix and use a transfer matrix approach to cascade multiple unit cells via matrix multiplication. This yields the complex propagation constant γ_m for the entire TWPA chip, as illustrated in figure 1. If needed, the model can be further refined by incorporating impedance transformers and bonding pads at the input and output of the amplifier. The resulting propagation constant is then used in equation (16) to simulate the evolution of the pump, signal, and idler tones along the TWPA.

One distinct advantage of this methodology is that it combines the rapid computational efficiency of the CMEs with the high-fidelity electromagnetic modelling capabilities of commercial *em* software packages. This hybrid approach enables more accurate prediction of TWPA performance by capturing the subtle electromagnetic effects of the STL, which become increasingly significant in designs involving hundreds of cascaded unit cells.

The flexibility of em simulation tools also provides a fast and simple platform for exploring and analysing different TWPA variants, thereby streamlining the process of designing bespoke TWPAs tailored to specific application requirements. Furthermore, this methodology offers a practical and efficient route to investigate more complex device architectures, such as multi-layer superconducting structures [57], and facilitates the integration of additional circuit elements such as on-chip filters or impedance transformers within the same framework. This opens the door to future developments beyond amplification, including functionalities such as frequency conversion [58], thereby broadening the utility and versatility of TWPA technology.

This methodology has already been demonstrated to accurately emulate the behaviour of a Ka-band KITWPA [59]. In the following, we extend this easy-to-use and computationally efficient framework to TWPAs based on JJs and DC-SQUIDs by modifying only the nonlinearity parameter, β_{nl}, in the CMEs (equations (16)). This extension is particularly valuable for junction-based TWPAs, where conventional modelling

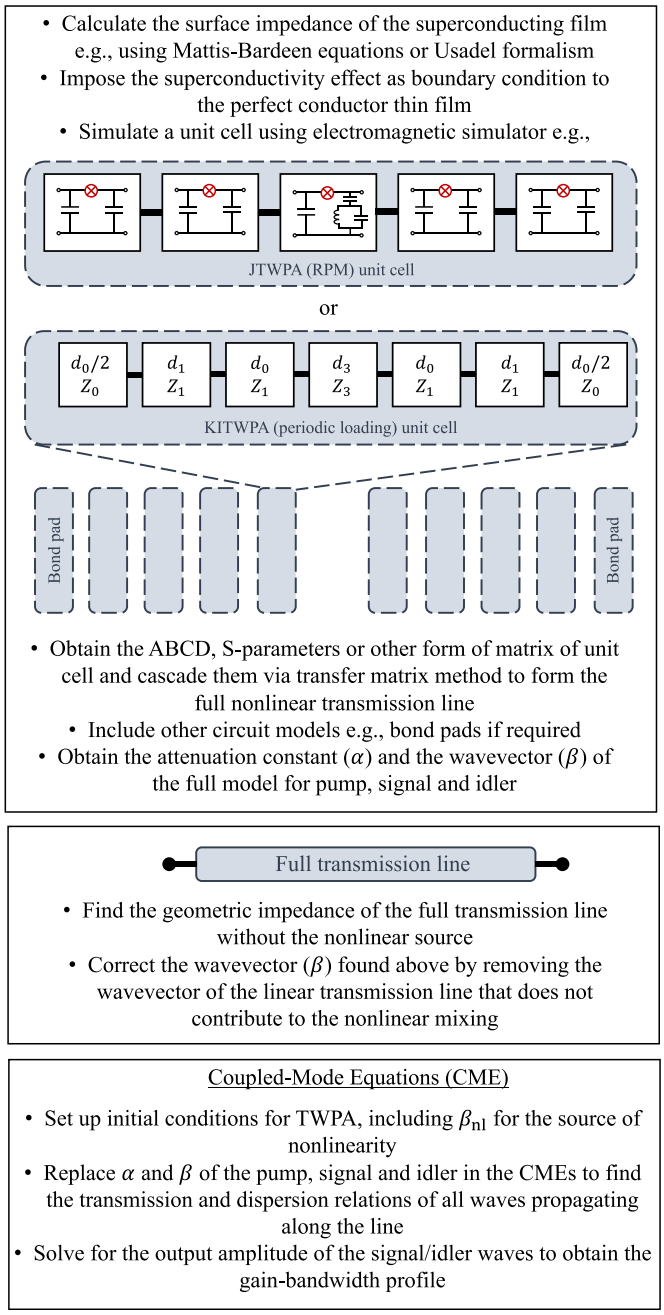

Figure 1. The sequence of computation procedures to simulate the behaviour of the TWPAs. A JTWPA with resonant phase matching (RPM) and a periodic loading KITWPA unit cell are used as an example. In the KITWPA unit cell, $d_{0,1,3}$ and $Z_{0,1,3}$ is the length and characteristic impedance of the primary transmission line section, the first loading section and the third loading section, respectively.

approaches often require re-deriving the CMEs from first principles for each variation in the equivalent circuit of the unit cell. In contrast, our framework remains agnostic to the underlying device architecture, enabling rapid exploration and evaluation of a broad range of TWPA designs with minimal computational overhead.

3. Framework validation

To validate the proposed framework for junction-based devices, this study focuses on reproducing the performance of two representative architectures: a Josephson JTWPA and a DC-SQUID-based TWPA. These devices were selected primarily due to the availability of sufficient design parameters reported in the literature, which enables meaningful benchmarking and reasonable replication of their reported performance. However, it should be noted that several critical details were omitted in the original publications, limiting the accuracy of direct reproduction of the measured data. These limitations will be discussed in detail in subsequent sections.

3.1. Bare-junctions JTWPAs

In [32], the authors introduced the first mathematical model describing a JTWPA using RPM technique to achieve exponential gain. Although this model successfully predicted the measured gain of a JTWPA device [22], it is limited to the design specifically presented in [32], and requires tedious re-derivation of the CME for any slight variation differing from the design. Here, we reproduce the gain curve of the theoretical model presented in [32] using the unit cell parameters given in the manuscript (summarised in table 2), and the proposed methodology. We calculate the `ABCD` matrix with a commercial circuit simulator (in our case Ansys® Circuit Designer), and cascading it 2000 times (the total number of cells in the design) to reproduce the device's result. From the cascaded `ABCD` matrix, we obtain the S_{21} parameter of the device as shown in the red line plotted in figure 2(a). From the phase of the S_{21}, we calculate the phase constant required to solve our CME. We remark the ripple effect in the S_{21} near the stopband calculated using our method compared to the mathematical model in [32] shown in black line in figure 2(a), which assumes translational symmetry. These ripples are originated from the interaction between the cascaded cells, and play an important roll in optimising the gain, since the placement of the pump frequency could prevent unwanted attenuation of the pump [49]. However, in this case the pump frequency ($f_p = 5.97$ GHz) almost coincides with a peak of transmission in the S_{21} profile, resulting in an almost optimal pumping scheme.

Using the calculated phase constant, we solve our CME (equations (16)) for the JTWPA in the DP4WM regime when pumping at $I_p/I_* = 0.54$, leading to the gain profile shown in figure 2(b) (red line). We observe a near perfect match with the gain profile obtained using the mathematical model presented in [32] (black line). The small deviation in bandwidth could result from the assumption of trivial junction capacitance not included in our model (see appendix A). Apart from these minor differences, the behaviour of the JTWPA is largely similar. Thereby, it demonstrates that the proposed methodology is viable for describing the behaviour of a JTWPA, even when comparing it to the results simulated using a different CME framework.

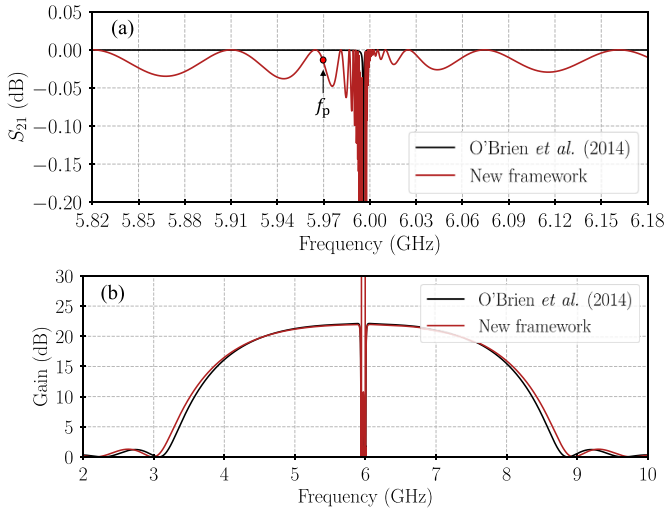

Figure 2. (a) The transmission profile (S_{21}) of the JTWPA design presented in [32] calculated using the translational symmetry assumption from the original framework (black) and cascading the unit cell (red) using our method. (b) Theoretical gain profile of JTWPA presented in [32] using the original framework (black) and the new framework introduce in this manuscript (red).

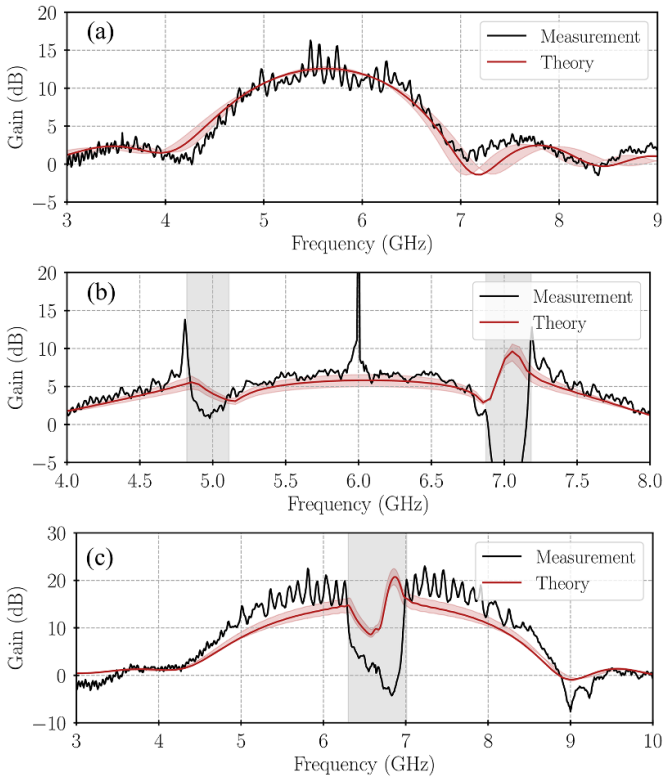

Figure 3. Gain profiles measured in [23, 48] compared to the predicted gain simulated using our framework. (a) Non-modulated SQUID array without magnetic flux using $I_p/I_* = 0.7$ for the theoretical calculation. The error margins correspond to a 10% variation of L_0. (b) Modulated SQUID array without magnetic flux using $I_p/I_* = 0.565$ for the theoretical calculation. (c) Non-modulated SQUID array with applied magnetic flux $\Phi/\Phi_0 = 0.2$ using $I_p/I_* = 0.685$ for the theoretical calculation. The shaded area shows the stopband regions where our calculation are not accurate due to nonphysical solutions (see appendix D). The error margins correspond to a 2% variation of L_0.

3.2. SQUID-based TWPAs

In [23], the authors reported the first successful operation of a SQUID-based TWPA operating in the DP4WM regime. The design comprised an array of symmetric DC-SQUIDs using aluminum-based junctions, with the electrical parameters of each unit cell modulated sinusoidally to create a stopband near 7 GHz, thereby satisfying the phase-matching condition. Prior to this work, they also fabricated and characterised similar SQUID arrays without periodic modulation—referred to hereafter as the non-modulated array—detailed in [48].

3.2.1. Non-modulated array. Using the cell circuit parameters from the non-modulated array in [48] (summarised in table 2), we compute the unit cell's ABCD matrix and cascade it 2063 times to match the number of cells in the actual device. Due to the microstrip transmission line architecture, the device exhibits significant frequency-dependent dielectric losses, as reported in section 6.3.2 of [48]. To account for this, we incorporate dielectric losses into our circuit model by adding a frequency-dependent shunt resistance to ground in the unit cell, given by $R_{\text{shunt}}(\omega) = 5 \times 10^{15}/\omega$. This yields a cascaded S_{21} response consistent with the measured transmission.

From the cascaded S_{21}, we extract the phase constant and solve the CME, resulting in the gain profile shown in figure 3(a). The authors in [48] note a 10% spread in measured junction inductance values across the wafer, which we incorporate as error margins in our theoretical calculations. Our simulated results show good agreement with the experimental data, with the minor discrepancies attributed to simplifications in the CME derivation and uncertainties in the device characteristics or operating conditions. The experimental and fitted parameters are for this case are summarised in table 3.

3.2.2. Modulated array. We next replicate the gain of the modulated SQUID array both with and without magnetic flux. First, we determine the appropriate values of R_{shunt} that result in the correct attenuation of the S_{21} profile, specifically $R_{\text{shunt}}(\omega) = 3.2 \times 10^{15}/\omega$ for the modulated SQUID array with magnetic flux $\Phi/\Phi_0 = 0.2$, and $R_{\text{shunt}}(\omega) = 4 \times 10^{15}/\omega$ for the same array without magnetic flux[4]. In [23] and [48], the authors observed a frequency shift in the stopband of the modulated SQUID arrays when high pump powers were applied. We attribute this effect to an increase in SQUID inductance with pump power, which leads to a higher phase constant. Using equation (2) for the unit cell inductance, we estimate the pump amplitude (I_p/I_*) by matching the stopband frequency in the measured gain profile.

[4] Since calibrated transmission data for the modulated-array design were not available, we estimated R_{shunt} by tuning its value — starting from that used in the non-modulated case — to achieve a better fit to the gain data. The discrepancy in R_{shunt} between the cases with and without an applied magnetic field may stem from magnetic-field-induced variations in Two-Level System (TLS) losses or the presence of magnetic impurities within the dielectric layer [65].

Table 2. Comparison of key design parameters for different JTWPA implementations. L_j and C_j are the junction/SQUID inductance and capacitance respectively, C_s is the shunt capacitance, C_c is the coupling capacitance of the RPM resonator, C_r and L_r are the capacitance and inductance of the RPM resonator respectively, γ and ζ are the Josephson and shunt capacitance modulation amplitude respectively, N_p the modulation period and N the number of junctions/SQUIDs.

	O'Brien *et al* [32]	Planat *et al* (non-mod., [48])	Planat *et al* (mod., [23])
L_j (pH)	100	88.1	60.5 ± 1.1
C_j (fF)	329	490	485
C_s (fF)	39	31	42.6
C_c (fF)	10	N/A	N/A
C_r (pF)	7.036	N/A	N/A
L_r (pH)	100	N/A	N/A
γ (%)	N/A	N/A	4.0
ζ (%)	N/A	N/A	3.2
N_p	N/A	N/A	40
N	2000	2063	2160

We then generate a wavevector with the unpumped value of the SQUID inductance, where the stopband is artificially shifted to lower frequencies accounting for the pump power (more details in appendix D), and solve the CME. The result obtained without applying magnetic flux, pumping the device at $f_p = 6$ GHz with $I_p/I_* = 0.565$, is plotted in figure 3(b). The error margins correspond to a 2% uncertainty in the measured SQUID inductance as indicated by the authors in [48]. Apart from the stopband regions (more details in appendix D), our frameworks manage to predict the general behaviour of the experimental gain curve.

Finally, we replicate the gain curve for the same device when pumped at $f_p = 6.635$ GHz with an applied magnetic flux of $\Phi/\Phi_0 = 0.2$, as shown in figure 3(c). The simulated result exhibits good agreement with the experimental gain profile. The experimental and fitted parameters for the modulated-array with and without applied magnetic field are summarised in table 3. While a perfect match with the measured data is difficult to achieve using the circuit parameters reported in [48] (table 2), our framework enables us to identify a set of L_0 and R_{shunt} values that result in an excellent fit.

Moreover, the ripple effect caused by impedance mismatches can be readily incorporated using a Fabry–Pérot cavity model, as described in [23]; further details are provided in appendix D. Given the relatively good agreement between our simulations and the experimental results, despite uncertainties in the unit cell parameter values, we believe that our framework offers a robust and versatile tool for the design and exploration of SQUID-based TWPAs.

3.3. KITWPAs

As discussed earlier, the mathematical framework presented here extends the CMEs originally developed for

Table 3. Experimental and fitted parameters of the SQUID JTWPA from [23, 48]. P_p and f_p are the pump power and frequency respectively, R_{shunt}/ω is the extracted shunt resistance per angular frequency, and I_p/I_* is the normalised pump current.

	Planat *et al* (non-mod., [48])	Planat *et al* (mod., [23]) $\Phi/\Phi_0 = 0$	Planat *et al* (mod., [23]) $\Phi/\Phi_0 = 0.2$
P_p (dBm) –exp.	Unknown	−70.3	−70.2
f_p (GHz) –exp.	5.6	6.0	6.635
R_{shunt}/ω $(\cdot 10^{15}\,\Omega)$ –fit	5.0	4.0	3.2
I_p/I_* –fit	0.7	0.565	0.685

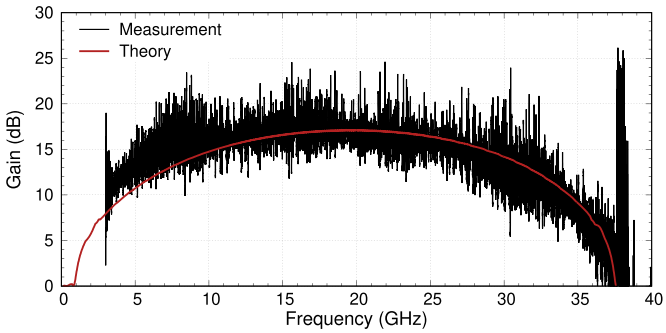

Figure 4. Gain profile measured (black) for a KITWPA operated in the DC3WM mode [60] compared to the predicted gain simulated using our framework (red). More details on the simulation are provided in [59].

KITWPAs [19]. For completeness, we reproduce results from [59], which model a KITWPA based on a 35-nm-thick NbTiN fishbone structure on a 100-μm tichk silicon substrate. This structure is covered by a 60-nm layer of amorphous silicon (a:Si) and capped with a 200-nm-thick NbTiN ground plane, forming an inverted microstrip geometry. Further details on the device layout can be found in [60].

We recreated the unit cell geometry of the KITWPA in HFSS, using the electromagnetic material parameters summarised in table 4. The target critical temperature $T_c = 12.5$ K, as reported in [60], was used as input. Following the procedure described in section 2, and using the current amplitudes stated in [60], we computed the expected gain profile. Figure 4 shows the resulting gain curve for a resistivity value $\rho = 168\,\mu\Omega\,$cm. This value is consistent with typical resistivity estimates for NbTiN, as discussed in [59]. A summary of the key simulation parameters is provided in table 4.

4. Non-conventional TWPA designs using the framework

Having demonstrated that our theoretical framework can predict the general gain-bandwidth behaviour of DP4WM

Table 4. Simulation parameters used for modeling the KITWPA device shown in figure 4. Dielectric constants ϵ_{Si} and $\epsilon_{a:Si}$ refer to silicon and amorphous silicon, respectively. T_c is the critical temperature, ρ the resistivity of the NbTiN film, I_* the nonlinear current scale, I_{dc} the applied DC bias, P_p the pump power, and f_p the pump frequency.

ε_{Si}	$\varepsilon_{a:Si}$	NbTiN T_c (K)	NbTiN ρ ($\mu\Omega$ cm)	I_* (mA)	I_{dc} (mA)	P_p (dBm)	f_p (GHz)
11.9	10.3	12.5	168.0	4.3	0.57	−27.5	38.8

JTWPAs, both non-dispersion-engineered and dispersion-engineered DC-SQUID TWPAs, as well as DC3WM KITWPAs, we now present an example application to a slightly non-conventional TWPA design: a NP4WM JTWPA. This design utilises two pump sources and adopts a periodic-loading dispersion engineering scheme, instead of the commonly used resonant phase-matching (RPM) approach, and operates in a higher frequency range of 20–40 GHz.

In most TWPAs, gain ripples arise from impedance mismatches between the 50 Ω environment and the nonlinear transmission line under strong pumping tone. Here, we revisit the concept of a JTWPA with periodic-loading dispersion engineering aimed at minimising these impedance mismatches [61]. While this strategy is broadly applicable to all wave-mixing regimes, we focus on a device operating in the non-degenerate pumped 4WM (NP4WM) regime.

Periodically loaded JTWPAs have been previously demonstrated [62, 63], typically implemented either by alternating the junction sizes between the main transmission line and the loading sections or by varying the shunt capacitance while keeping the junction parameters fixed. A unique feature of our design is that the main transmission line consists of a linear, passive material, specifically low-KI- niobium in this example. This ensures a constant characteristic impedance (Z_0), even under strong pumping, leading to better impedance matching with the 50 Ω input/output environment and minimising gain ripples due to reflections. The overall design concept and unit cell layout are illustrated in figures 5(a) and (b).

In this architecture, the loading sections comprise sets of JJs embedded periodically along the transmission line; in this case a CPW. These junctions locally modify Z_0 and simultaneously act as the nonlinear medium for wave mixing. Their periodic placement introduces stopbands in the transmission line, enabling engineered excursions in the dispersion relation and suppressing unwanted harmonics–functionally similar to conventional periodic loading schemes, as shown in figure 5(c). Capacitive stubs are added at these loading points to locally tune Z_0 and thereby control the width and depth of the stopbands, directly influencing the amplitude of the dispersion excursion. The plasma resonance frequency of the junctions is also engineered to enhance nonlinear dispersion above the primary stopband (∼60 GHz), further suppressing higher pump harmonics.

A significant benefit of this design is that small variations in Z_0 at the loading sections under pumping have minimal impact on gain-bandwidth performance and ripple behaviour. Eliminating resonators also simplifies fabrication, increases yield, and reduces device footprint. However, this scheme necessitates a significantly longer transmission line, due to the low inductance of the main sections. As such, microstrip transmission lines are advantageous for this application[5]. Nevertheless, due to current fabrication constraints, we implement the design using CPW, with plans to transition to microstrip structures in future work.

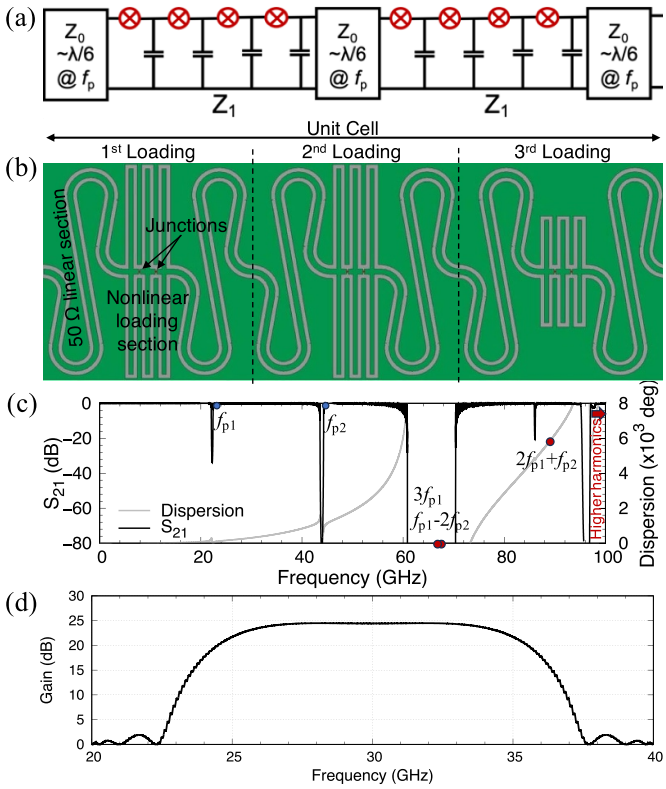

Figure 5. (a) Periodically-loaded JTWPA operating in the NP4WM regime. (b) Layout of the fundamental cells cascaded to form the JTWPA. The junctions are expected to have a critical current of 7 μA and size of 0.5 μm, resulting in the junction capacitance of 36.81 fF and inductance of 47.02 pH, with a plasma resonance frequency around 121 GHz. (c) The stopbands structures and the cumulative dispersion relation of the periodically-loaded JTWPA optimised to suppress unwanted higher pumps harmonics. (d) Gain-bandwidth product of the JTWPA with the first pump frequency located at 22.5 GHz and the second pump frequency at 44.5 GHz. Both pumps's amplitude were set at $0.28I_*$.

We simulated the unit cells of the design using HFSS, assuming a 500-μm thick silicon substrate and a niobium

[5] It is generally more difficult to implement coupled resonators for RPM in microstrip geometry, making periodic loading a more natural dispersion engineering approach. Conversely, CPW geometries are more amenable to RPM schemes.

Table 5. Key parameters used in the simulation of the non-conventional DP4WM JTWPA. $T_{c,\,Nb}$ is the critical temperature of the Nb film, ϵ_{Si} the relative permittivity of the Si substrate. L_j and C_j are the junction inductance and capacitance, respectively. N_{cells} is the number of unit cells, f_{p_1} and f_{p_2} are the pump frequencies, and I_{p_1}/I_* and I_{p_2}/I_* denote the normalised pump currents.

$T_{c,\,Nb}$ (K)	ε_{Si}	L_j (pH)	C_j (fF)	N_{cells}	f_{p_1} (GHz)	f_{p_2} (GHz)	I_{p_1}/I_*	I_{p_2}/I_*
9.2	11.9	47.02	36.81	200	22.5	44.5	0.28	0.28

(Nb) CPW with trilayer (Nb/Al-AlO_x/Nb) junctions. Then, we use the steps described in section 2 to obtain the gain profile of this design operated in the NP4WM regime. The main design parameters are summarised in table 5. The predicted NP4WM gain profile is presented in figure 5(d). Simulating the gain behaviour of such devices poses a challenge for conventional JTWPA CME models and typically requires computational-intensive and time-consuming SPICE simulations. In contrast, the framework introduced in this manuscript offers a much more computationally efficient and versatile approach for exploring advanced JTWPAs, as highlighted by this example.

5. Conclusion

Various theoretical models have been developed to describe the behaviour of different types of TWPAs. In this manuscript, we have presented a generalised mathematical framework capable of modelling all symmetric $\chi^{(3)}$ TWPAs, including those based on JJs, high kinetic inductance superconducting films, and symmetric DC-SQUIDs. Our approach is applicable across different mixing regimes: non-degenerate four-wave mixing (NP4WM), degenerate four-wave mixing (DP4WM), and DC three-wave mixing (DC3WM).

This framework requires only the complex propagation constant γ_m and the ratio I_p/I_* (along with I_{dc} in the DC3WM case) to fully characterise a TWPA. By leveraging commercial electromagnetic *em* simulators to extract γ_m, our method offers a flexible, computationally efficient means to predict amplifier performance. We have validated the framework against experimental data from both a Josephson-junction-based TWPA and a DC-SQUID-based TWPA reported in the literature.

While the current formulation is limited to symmetric TWPAs with $\chi^{(3)}$ nonlinearities, the underlying methodology could be adapted to $\chi^{(2)}$ systems, potentially establishing a foundation for a more general modelling framework. Future directions could also include incorporating higher-order terms in the nonlinear inductance beyond the first-order Taylor expansion currently employed. Such refinements would relax the $I \ll I_*$ constraint, enabling more accurate modelling of TWPA behaviour at higher pump powers—regime where alternative simulation techniques to the CMEs, such as harmonic balance or time-domain methods, become increasingly computationally demanding. Despite these limitations, the simplicity and versatility of the present approach make it particularly well-suited for the design, exploration, and optimisation of increasingly complex TWPA architectures tailored to specific applications.

Data availability statement

All data that support the findings of this study are included within the article (and any supplementary files).

Acknowledgments

We thank Luca Planat and Nicolas Roch for providing the measured data of the DC-SQUID TWPA device presented in this manuscript. This research was supported by the MERAC foundation, the European Research Council (ERC) under the European Union's Horizon 2020 research and innovation programme with Grant Agreement No. [803862] (Project [SPA4AstroQIT]) and the UKRI Quantum Technology for Fundamental Physics programme under the project Quantum Sensor for Hidden Sector. J Navarro Montilla's D.Phil. studentship is supported by the UK Science and Technology Facilities Council and the Foley-Bejar Scholarship from Balliol College, Oxford.

Appendix A. Negligible effect of junction capacitance

JJs operated below the critical temperature of the superconducting electrodes are often electrically modelled as a capacitor (C_j) and a nonlinear inductor in parallel—with the inductance given by equation (5). However, in the STL lumped-element circuit model used in our CME derivation, the effect of C_j is neglected. The equivalent impedance of the capacitor (Z_C) and inductor (Z_L) in the junction model is defined as:

$$\begin{aligned} Z_L &= i\omega L_j \\ Z_C &= \frac{1}{i\omega C_j}. \end{aligned} \tag{A1}$$

For all the JTWPAs published to date, the order of magnitude in the international units (IU) system is $10^{-14}\text{F} \lesssim C_j \lesssim 10^{-13}$ F and $10^{-11}\text{H} \lesssim L_j \lesssim 10^{-10}$ H. Therefore, $|Z_L| \ll |Z_C|$, hence most of the current flows through L_j, and C_j can be safely neglected.

Appendix B. Derivation of CME coefficients

Degenerate-pump 4WM.— Assuming a degenerated pump tone is applied to a TWPA i.e. $f_{\rm p} = f_{\rm p_1} = f_{\rm p_2}$, and to preserve the total energy in the system:

$$\begin{aligned} P_{\rm p_1} + P_{\rm p_2} &= P_{\rm p} \\ I_{\rm p_1}^2 R + I_{\rm p_2}^2 R &= I_{\rm p}^2 R \\ I_{\rm p_1}^2 + I_{\rm p_2}^2 &= I_{\rm p}^2, \end{aligned} \tag{B1}$$

therefore,

$$\begin{aligned} A_{\rm p_1}^2(z)\,{\rm e}^{2\left({\rm i}\omega_{\rm p_1}t-\gamma_{\rm p_1}z\right)} + A_{\rm p_2}^2(z)\,{\rm e}^{2\left({\rm i}\omega_{\rm p_2}t-\gamma_{\rm p_2}z\right)} \\ = A_{\rm p}^2(z)\,{\rm e}^{2({\rm i}\omega_{\rm p}t-\gamma_{\rm p}z)}. \end{aligned}$$

This condition can only be met if $A_{\rm p_1} = A_{\rm p_2} = A_{\rm p}/\sqrt{2}$, $\omega_{\rm p_1} = \omega_{\rm p_2} = \omega_{\rm p}$, $\gamma_{\rm p_1} = \gamma_{\rm p_2} = \gamma_{\rm p}$ i.e. $\alpha_{\rm p_1} = \alpha_{\rm p_2} = \alpha_{\rm p}$ and $\beta_{\rm p_1} = \beta_{\rm p_2} = \beta_{\rm p}$.

Deriving the CME with a degenerated pump tone, we obtain the following set of equations:

$$\gamma_{\rm p}\frac{\partial A_{\rm p}(z)}{\partial z} = \frac{\beta_{\rm nl}\beta_{\rm p}^2}{8I_*^2}\left[A_{\rm p}\left(A_{\rm p}A_{\rm p}^*{\rm e}^{-2\alpha_{\rm p}z} + 2A_{\rm s}A_{\rm s}^*{\rm e}^{-2\alpha_{\rm s}z} + 2A_{\rm i}A_{\rm i}^*{\rm e}^{-2\alpha_{\rm i}z}\right) + 2A_{\rm p}^*A_{\rm s}A_{\rm i}{\rm e}^{-(\alpha_{\rm s}+\alpha_{\rm i})z}{\rm e}^{-{\rm i}\Delta_\beta z}\right] \tag{B2a}$$

$$\gamma_{\rm s}\frac{\partial A_{\rm s}(z)}{\partial z} = \frac{\beta_{\rm nl}\beta_{\rm s}^2}{8I_*^2}\left[A_{\rm s}\left(2A_{\rm p}A_{\rm p}^*{\rm e}^{-2\alpha_{\rm p}z} + A_{\rm s}A_{\rm s}^*{\rm e}^{-2\alpha_{\rm s}z} + 2A_{\rm i}A_{\rm i}^*{\rm e}^{-2\alpha_{\rm i}z}\right) + A_{\rm p}^2A_{\rm i}^*{\rm e}^{-(2\alpha_{\rm p}-\alpha_{\rm s}+\alpha_{\rm i})z}{\rm e}^{{\rm i}\Delta_\beta z}\right] \tag{B2b}$$

$$\gamma_{\rm i}\frac{\partial A_{\rm i}(z)}{\partial z} = \frac{\beta_{\rm nl}\beta_{\rm i}^2}{8I_*^2}\left[A_{\rm i}\left(2A_{\rm p}A_{\rm p}^*{\rm e}^{-2\alpha_{\rm p}z} + 2A_{\rm s}A_{\rm s}^*{\rm e}^{-2\alpha_{\rm s}z} + A_{\rm i}A_{\rm i}^*{\rm e}^{-2\alpha_{\rm i}z}\right) + A_{\rm p}^2A_{\rm s}^*{\rm e}^{-(2\alpha_{\rm p}+\alpha_{\rm s}-\alpha_{\rm i})z}{\rm e}^{{\rm i}\Delta_\beta z}\right] \tag{B2c}$$

which implies $\eta_{\rm p_{11}} = 0$ and $\eta_{\rm p_{22}} = 1$.

With the undepleted pump assumption, the CMEs can be further reduced and can be solved analytically. Similarly to appendix C, we find the reduced set of CMEs:

$$A_{\rm p}(z) - A_{0,\rm p}{\rm e}^{{\rm i}\varphi_{\rm p}z} = 0 \tag{B3a}$$

$$\frac{\partial a_{\rm s}(z)}{\partial z} - i\kappa_{\rm s}a_{\rm i}^*(z)\,{\rm e}^{{\rm i}\Delta_\phi z} = 0 \tag{B3b}$$

$$\frac{\partial a_{\rm i}(z)}{\partial z} - i\kappa_{\rm i}a_{\rm s}^*(z)\,{\rm e}^{{\rm i}\Delta_\phi z} = 0 \tag{B3c}$$

where

$$\begin{aligned} \Delta_\phi &= \Delta_\beta + 2\varphi_{\rm p} - \varphi_{\rm s} - \varphi_{\rm i} \\ &= 2\beta_{\rm p} - \beta_{\rm s} - \beta_{\rm i} - 2\varphi_{\rm p} - \varphi_{\rm s} - \varphi_{\rm i} \\ \kappa_{\rm s} &= \varphi_{\rm s}'{\rm e}^{(\alpha_{\rm s}-\alpha_{\rm i})z} \qquad \kappa_{\rm i} = \varphi_{\rm i}'{\rm e}^{(-\alpha_{\rm s}+\alpha_{\rm i})z} \\ \varphi_{\rm s}' &= \varphi_{\rm s}/2 \qquad \varphi_{\rm i}' = \varphi_{\rm i}/2 \\ \varphi_{\rm s} &= -i\frac{\beta_{\rm nl}\beta_{\rm s}^2}{4I_*^2\gamma_{\rm s}}(2\varphi_{\rm pp}) \qquad \varphi_{\rm i} = -i\frac{\beta_{\rm nl}\beta_{\rm i}^2}{4I_*^2\gamma_{\rm i}}(2\varphi_{\rm pp}) \\ \varphi_{\rm pp} &= \frac{|A_{0,\rm p}|^2}{2}{\rm e}^{-2\alpha_{\rm p}z}. \end{aligned}$$

For the lossless case, all the α_m are set to zero. The solution to the signal and idler CMEs are given as

$$\begin{aligned} a_{\rm s}(z) = \left\{\left[\cosh(gz) - \frac{{\rm i}\Delta_\phi}{2g}\sinh(gz)\right]a_{\rm s}(0)\right. \\ \left. + \left[\frac{i\kappa_{\rm s}}{g}\sinh(gz)\right]a_{\rm i}(0)\right\}{\rm e}^{{\rm i}\Delta_\phi z/2} \end{aligned} \tag{B4a}$$

$$\begin{aligned} a_{\rm i}(z) = \left\{\left[\cosh(gz) - \frac{{\rm i}\Delta_\phi}{2g}\sinh(gz)\right]a_{\rm i}(0)\right. \\ \left. + \left[\frac{i\kappa_{\rm i}}{g}\sinh(gz)\right]a_{\rm s}(0)\right\}{\rm e}^{{\rm i}\Delta_\phi z/2} \end{aligned} \tag{B4b}$$

where $g = \sqrt{\kappa_{\rm s}\kappa_{\rm i} - \frac{\Delta_\phi^2}{4}}$.

DC-bias 3WM.— For the DC-bias 3WM case, we can replace $\frac{1}{2}A_{\rm p_1}(z){\rm e}^{({\rm i}\omega_{\rm p_1}t-\gamma_{\rm p_1}z)} = \frac{1}{2}A_{\rm p}(z){\rm e}^{({\rm i}\omega_{\rm p}t-\gamma_{\rm p}z)}$ and the second pump tone by a DC current i.e. $|A_{\rm p_2}(z)| = 2I_{\rm dc}$. The factor of 2 is added to account for the conjugate of $A_{\rm p_2}(z)$ ensuring the total energy in the system is conserved. Furthermore, since there is no oscillation of the current in a DC signal, $\gamma_{\rm p_2} = \omega_{\rm p_2} = \alpha_{\rm p_2} = 0$.

Following the procedure above, but considering a DC signal and a pump tone, we derive the following set of CME:

$$\begin{aligned} \gamma_{\rm p}\frac{\partial A_{\rm p}(z)}{\partial z} = \frac{\beta_{\rm nl}\beta_{\rm p}^2}{8I_*^2}\left[A_{\rm p}\left(A_{\rm p}A_{\rm p}^*{\rm e}^{-2\alpha_{\rm p}z}\right.\right. \\ \left. + 2A_{\rm s}A_{\rm s}^*{\rm e}^{-2\alpha_{\rm s}z} + 2A_{\rm i}A_{\rm i}^*{\rm e}^{-2\alpha_{\rm i}z} + 4I_{\rm dc}^2\right) \\ \left. + 4I_{\rm dc}A_{\rm s}A_{\rm i}{\rm e}^{\left(2\alpha_{\rm p}-\Delta_{\alpha_3}\right)z}{\rm e}^{-{\rm i}\Delta_{\beta_3}z}\right] \end{aligned} \tag{B5a}$$

$$\begin{aligned} \gamma_{\rm s}\frac{\partial A_{\rm s}(z)}{\partial z} = \frac{\beta_{\rm nl}\beta_{\rm s}^2}{8I_*^2}\left[A_{\rm s}\left(2A_{\rm p}A_{\rm p}^*{\rm e}^{-2\alpha_{\rm p}z} + A_{\rm s}A_{\rm s}^*{\rm e}^{-2\alpha_{\rm s}z}\right.\right. \\ \left. + 2A_{\rm i}A_{\rm i}^*{\rm e}^{-2\alpha_{\rm i}z} + 4I_{\rm dc}^2\right) \\ \left. + 4I_{\rm dc}A_{\rm p}A_{\rm i}^*{\rm e}^{\left(2\alpha_{\rm s}-\Delta_{\alpha_3}\right)z}{\rm e}^{{\rm i}\Delta_{\beta_3}z}\right] \end{aligned} \tag{B5b}$$

$$\gamma_{\mathrm{i}}\frac{\partial A_{\mathrm{i}}(z)}{\partial z}=\frac{\beta_{\mathrm{nl}}\beta_{\mathrm{i}}^{2}}{8I_{*}^{2}}\left[A_{\mathrm{i}}\left(2A_{\mathrm{p}}A_{\mathrm{p}}^{*}\mathrm{e}^{-2\alpha_{\mathrm{p}}z}+A_{\mathrm{s}}A_{\mathrm{s}}^{*}\mathrm{e}^{-2\alpha_{\mathrm{s}}z}+2A_{\mathrm{i}}A_{\mathrm{i}}^{*}\mathrm{e}^{-2\alpha_{\mathrm{i}}z}+4I_{\mathrm{dc}}^{2}\right)+4I_{\mathrm{dc}}A_{\mathrm{p}}A_{\mathrm{s}}^{*}\mathrm{e}^{\left(2\alpha_{\mathrm{i}}-\Delta_{\alpha_3}\right)z}\mathrm{e}^{\mathrm{i}\Delta_{\beta_3}z}\right] \tag{B5c}$$

implying $\eta_{\mathrm{p}_{11}}=1$ and $\eta_{\mathrm{p}_{22}}=\frac{1}{2}$. $\eta_{\mathrm{p}_{22}}=\frac{1}{2}$ because there is no self interaction in the DC signal with its non-existent conjugate i.e. there is no backward moving wave associated to a DC signal, hence the self-phase modulation is half compared with conventional oscillating tones like the pump, signal or idler.

Assuming the pump is undepleted, the CME is further reduced analytically:

$$A_{\mathrm{p}}(z)-A_{0,\mathrm{p}}\mathrm{e}^{\mathrm{i}\varphi_{\mathrm{p}}z}=0 \tag{B6a}$$

$$\frac{\partial a_{\mathrm{s}}(z)}{\partial z}-i\kappa_{\mathrm{s}}a_{\mathrm{i}}^{*}(z)\,\mathrm{e}^{\mathrm{i}\Delta_{\phi_3}z}=0 \tag{B6b}$$

$$\frac{\partial a_{\mathrm{i}}(z)}{\partial z}-i\kappa_{\mathrm{i}}a_{\mathrm{s}}^{*}(z)\,\mathrm{e}^{\mathrm{i}\Delta_{\phi_3}z}=0, \tag{B6c}$$

where

$$\begin{aligned}
\Delta_{\phi_3}&=\Delta_{\beta_3}+\varphi_{\mathrm{p}}-\varphi_{\mathrm{s}}-\varphi_{\mathrm{i}}\\
&=\beta_{\mathrm{p}}-\beta_{\mathrm{s}}-\beta_{\mathrm{i}}-\varphi_{\mathrm{p}}-\varphi_{\mathrm{s}}-\varphi_{\mathrm{i}}\\
\kappa_{\mathrm{s}}&=\varphi_{\mathrm{s}}'\mathrm{e}^{(\alpha_{\mathrm{s}}-\alpha_{\mathrm{i}})z} & \kappa_{\mathrm{i}}&=\varphi_{\mathrm{i}}'\mathrm{e}^{(-\alpha_{\mathrm{s}}+\alpha_{\mathrm{i}})z}\\
\varphi_{\mathrm{s}}'&=-i\frac{\beta_{\mathrm{nl}}\beta_{\mathrm{s}}^{2}}{4I_{*}^{2}\gamma_{\mathrm{s}}}\varphi_{\mathrm{p,dc}} & \varphi_{\mathrm{i}}'&=-i\frac{\beta_{\mathrm{nl}}\beta_{\mathrm{i}}^{2}}{4I_{*}^{2}\gamma_{\mathrm{i}}}\varphi_{\mathrm{p,dc}}\\
\varphi_{\mathrm{s}}&=-i\frac{\beta_{\mathrm{nl}}\beta_{\mathrm{s}}^{2}}{4I_{*}^{2}\gamma_{\mathrm{s}}}\left(\varphi_{\mathrm{pp}}+\varphi_{\mathrm{dc}}\right) & \varphi_{\mathrm{i}}&=-i\frac{\beta_{\mathrm{nl}}\beta_{\mathrm{i}}^{2}}{4I_{*}^{2}\gamma_{\mathrm{i}}}\left(\varphi_{\mathrm{pp}}+\varphi_{\mathrm{dc}}\right)\\
\varphi_{\mathrm{p,dc}}&=2I_{\mathrm{dc}}A_{0,\mathrm{p}}\mathrm{e}^{-\alpha_{\mathrm{p}}z} & \varphi_{\mathrm{pp}}&=\frac{|A_{0,\mathrm{p}}|^{2}}{2}\mathrm{e}^{-2\alpha_{\mathrm{p}}z},
\end{aligned}$$

where all α_m are set to zero for the lossless case. The solution to the signal and idler CMEs are given as

$$a_{\mathrm{s}}(z)=\left\{\left[\cosh(gz)-\frac{\mathrm{i}\Delta_{\phi}}{2g}\sinh(gz)\right]a_{\mathrm{s}}(0)+\left[\frac{i\kappa_{\mathrm{s}}}{g}\sinh(gz)\right]a_{\mathrm{i}}(0)\right\}\mathrm{e}^{\mathrm{i}\Delta_{\phi_3}z/2} \tag{B7a}$$

$$a_{\mathrm{i}}(z)=\left\{\left[\cosh(gz)-\frac{\mathrm{i}\Delta_{\phi}}{2g}\sinh(gz)\right]a_{\mathrm{i}}(0)+\left[\frac{i\kappa_{\mathrm{i}}}{g}\sinh(gz)\right]a_{\mathrm{s}}(0)\right\}\mathrm{e}^{i\Delta_{\phi_3}z/2}, \tag{B7b}$$

where $g=\sqrt{\kappa_{\mathrm{s}}\kappa_{\mathrm{i}}-\frac{\Delta_{\phi_3}^{2}}{4}}$.

Appendix C. Derivation of analytical solutions

Equation (16) can be solved analytically to provide a better understanding of the devices operation. Considering a low-loss STL, the term $\frac{G}{\omega_m C}$ is negligible. Assuming the pump tones are undepleted thought the STL, and the their amplitude are much stronger than the signal and idler wave i.e. $A_{\mathrm{p}_1}, A_{\mathrm{p}_2}\gg A_{\mathrm{s}}\,\&\,A_{\mathrm{i}}$, the pump equations reduces to

$$\frac{\partial A_{\mathrm{p}_1}(z)}{\partial z}-i\varphi_{\mathrm{p}_1}'A_{\mathrm{p}_1}=0 \tag{C1a}$$

$$\frac{\partial A_{\mathrm{p}_2}(z)}{\partial z}-i\varphi_{\mathrm{p}_2}'A_{\mathrm{p}_2}=0, \tag{C1b}$$

where

$$\varphi_{\mathrm{p}_1}'=-i\frac{\beta_{\mathrm{nl}}\beta_{\mathrm{p}_1}^{2}}{8I_{*}^{2}\gamma_{\mathrm{p}_1}}\left[\eta_{\mathrm{p}_{11}}A_{\mathrm{p}_1}A_{\mathrm{p}_1}^{*}\mathrm{e}^{-2\alpha_{\mathrm{p}_1}z}+2\eta_{\mathrm{p}_{22}}A_{\mathrm{p}_2}A_{\mathrm{p}_2}^{*}\mathrm{e}^{-2\alpha_{\mathrm{p}_2}z}\right]$$

$$\varphi_{\mathrm{p}_2}'=-i\frac{\beta_{\mathrm{nl}}\beta_{\mathrm{p}_2}^{2}}{8I_{*}^{2}\gamma_{\mathrm{p}_2}}\left[2\eta_{\mathrm{p}_{11}}A_{\mathrm{p}_1}A_{\mathrm{p}_1}^{*}\mathrm{e}^{-2\alpha_{\mathrm{p}_1}z}+\eta_{\mathrm{p}_{22}}A_{\mathrm{p}_2}A_{\mathrm{p}_2}^{*}\mathrm{e}^{-2\alpha_{\mathrm{p}_2}z}\right].$$

The solution of these partial differential equation is in the form of a plane wave $A_{\mathrm{p}_1}(z)=C\mathrm{e}^{\mathrm{i}\varphi' z}$, where C is a constant. Using the pump amplitude at $z=0$ as a boundary condition, we can solve for C, then $A_{\mathrm{p}_1}(0)=C=A_{0,\mathrm{p}_1}$. Hence, the solution for the pump tones is:

$$A_{\mathrm{p}_1}(z)=A_{0,\mathrm{p}_1}\mathrm{e}^{\mathrm{i}\varphi_{\mathrm{p}_1}z} \tag{C2a}$$

$$A_{\mathrm{p}_2}(z)=A_{0,\mathrm{p}_2}\mathrm{e}^{\mathrm{i}\varphi_{\mathrm{p}_2}z}, \tag{C2b}$$

where

$$\begin{aligned}
\varphi_{\mathrm{p}_1}&=-i\frac{\beta_{\mathrm{nl}}\beta_{\mathrm{p}_1}^{2}}{8I_{*}^{2}\gamma_{\mathrm{p}_1}}\left(\varphi_{\mathrm{p}_{11}}+2\varphi_{\mathrm{p}_{22}}\right)\\
\varphi_{\mathrm{p}_2}&=-i\frac{\beta_{\mathrm{nl}}\beta_{\mathrm{p}_2}^{2}}{8I_{*}^{2}\gamma_{\mathrm{p}_2}}\left(2\varphi_{\mathrm{p}_{11}}+\varphi_{\mathrm{p}_{22}}\right)\\
\varphi_{\mathrm{p}_{11}}&=\eta_{\mathrm{p}_{11}}A_{0,\mathrm{p}_1}A_{0,\mathrm{p}_1}^{*}\mathrm{e}^{-2\alpha_{\mathrm{p}_1}z}\\
\varphi_{\mathrm{p}_{22}}&=\eta_{\mathrm{p}_{22}}A_{0,\mathrm{p}_2}A_{0,\mathrm{p}_2}^{*}\mathrm{e}^{-2\alpha_{\mathrm{p}_2}z}.
\end{aligned}$$

By replacing equations (C2) in the simplified signal equation resulting from the aforementioned assumptions, we obtain:

$$\frac{\partial A_{\mathrm{s}}(z)}{\partial z}=i\varphi_{\mathrm{s}}A_{\mathrm{s}}+i\varphi_{\mathrm{s}}'A_{\mathrm{i}}^{*}\mathrm{e}^{(\alpha_{\mathrm{s}}-\alpha_{\mathrm{i}})z}\mathrm{e}^{\mathrm{i}\left(\Delta_{\beta}+\varphi_{\mathrm{p}_1}+\varphi_{\mathrm{p}_2}\right)z} \tag{C3a}$$

$$\frac{\partial A_{\mathrm{i}}(z)}{\partial z}=i\varphi_{\mathrm{i}}A_{\mathrm{i}}+i\varphi_{\mathrm{i}}'A_{\mathrm{s}}^{*}\mathrm{e}^{(-\alpha_{\mathrm{s}}+\alpha_{\mathrm{i}})z}\mathrm{e}^{\mathrm{i}\left(\Delta_{\beta}+\varphi_{\mathrm{p}_1}+\varphi_{\mathrm{p}_2}\right)z}, \tag{C3b}$$

where

$$\varphi_{\mathrm{s}}=-i\frac{\beta_{\mathrm{nl}}\beta_{\mathrm{s}}^{2}}{4I_{*}^{2}\gamma_{\mathrm{s}}}\left(\varphi_{\mathrm{p}_{11}}+\varphi_{\mathrm{p}_{22}}\right),\ \text{and}\ \varphi_{\mathrm{s}}'=-i\frac{\beta_{\mathrm{nl}}\beta_{\mathrm{s}}^{2}}{4I_{*}^{2}\gamma_{\mathrm{s}}}\varphi_{\mathrm{p}_{12}}$$

$$\varphi_{\mathrm{i}}=-i\frac{\beta_{\mathrm{nl}}\beta_{\mathrm{i}}^{2}}{4I_{*}^{2}\gamma_{\mathrm{i}}}\left(\varphi_{\mathrm{p}_{11}}+\varphi_{\mathrm{p}_{22}}\right),\ \text{and}\ \varphi_{\mathrm{s}}'=-i\frac{\beta_{\mathrm{nl}}\beta_{\mathrm{i}}^{2}}{4I_{*}^{2}\gamma_{\mathrm{i}}}\varphi_{\mathrm{p}_{12}}.$$

Assuming that the solution for the above CMEs will be in the form of $A_{\mathrm{s}}(z)=a_{\mathrm{s}}(z)\mathrm{e}^{\mathrm{i}\varphi_{\mathrm{s}}z}$ and $A_{\mathrm{i}}(z)=a_{\mathrm{i}}(z)\mathrm{e}^{\mathrm{i}\varphi_{\mathrm{i}}z}$, replacing the equations (C3), we obtain:

$$\frac{\partial a_{\mathrm{s}}(z)}{\partial z}-i\kappa_{\mathrm{s}}a_{\mathrm{i}}^{*}(z)\,\mathrm{e}^{\mathrm{i}\Delta_{\phi}z}=0 \tag{C4a}$$

$$\frac{\partial a_{\mathrm{i}}(z)}{\partial z}-i\kappa_{\mathrm{i}}a_{\mathrm{s}}^{*}(z)\,\mathrm{e}^{\mathrm{i}\Delta_{\phi}z}=0, \tag{C4b}$$

where

$$\kappa_{\mathrm{s}}=\varphi_{\mathrm{s}}'\mathrm{e}^{(\alpha_{\mathrm{s}}-\alpha_{\mathrm{i}})z},\ \text{and}\ \kappa_{\mathrm{i}}=\varphi_{\mathrm{i}}'\mathrm{e}^{(-\alpha_{\mathrm{s}}+\alpha_{\mathrm{i}})z}$$

$$\varphi_{\mathrm{p}_{12}}=A_{0,\mathrm{p}_1}A_{0,\mathrm{p}_2}^{*}\mathrm{e}^{-\left(\alpha_{\mathrm{p}_1}+\alpha_{\mathrm{p}_2}\right)z}$$

Table 6. Parameters of the CME for the non-degenerate pump 4-wave mixing (NP4WM), degenerate pump 4-wave mixing (DP4WM) and the DC-bias 3-wave mixing (DC3WM) regimes of a TWPA.

	NP4WM	DP4WM	DC3WM
$A_{\mathrm{p}_1}(z)$	$A_{0,\mathrm{p}_1}\mathrm{e}^{\mathrm{i}\varphi_{\mathrm{p}_1}z}$	$A_{0,\mathrm{p}}\mathrm{e}^{i\varphi_{\mathrm{p}}z}$	$A_{0,\mathrm{p}}\mathrm{e}^{\mathrm{i}\varphi_{\mathrm{p}}z}$
$A_{\mathrm{p}_2}(z)$	$A_{0,\mathrm{p}_2}\mathrm{e}^{i\varphi_{\mathrm{p}_2}z}$		
φ_{p_1}	$-i\frac{\beta_{\mathrm{nl}}\beta_{\mathrm{p}_1}^2}{8I_*^2\gamma_{\mathrm{p}_1}}(\varphi_{\mathrm{p}_{11}}+2\varphi_{\mathrm{p}_{22}})$	$\varphi_{\mathrm{p}}=-i\frac{\beta_{\mathrm{nl}}\beta_{\mathrm{p}}^2}{8I_*^2\gamma_{\mathrm{p}}}(2\varphi_{pp})$	$\varphi_{\mathrm{p}}=-i\frac{\beta_{\mathrm{nl}}\beta_{\mathrm{p}}^2}{8I_*^2\gamma_{\mathrm{p}}}(\varphi_{pp}+2\varphi_{\mathrm{dc}})$
φ_{p_2}	$-i\frac{\beta_{\mathrm{nl}}\beta_{\mathrm{p}_2}^2}{8I_*^2\gamma_{\mathrm{p}_2}}(2\varphi_{\mathrm{p}_{11}}+\varphi_{\mathrm{p}_{22}})$		
$\varphi_{\mathrm{p}_{11}}$	$\eta_{\mathrm{p}_{11}}A_{0,\mathrm{p}_1}A_{0,\mathrm{p}_1}^*\mathrm{e}^{-2\alpha_{\mathrm{p}_1}z}$	$\varphi_{pp}=\frac{\lvert A_{0,\mathrm{p}}\rvert^2}{2}\mathrm{e}^{-2\alpha_{\mathrm{p}}z}$	$\varphi_{pp}=A_{0,\mathrm{p}}A_{0,\mathrm{p}}^*\mathrm{e}^{-2\alpha_{\mathrm{p}}z}$
$\varphi_{\mathrm{p}_{22}}$	$\eta_{\mathrm{p}_{22}}A_{0,\mathrm{p}_2}A_{0,\mathrm{p}_2}^*\mathrm{e}^{-2\alpha_{\mathrm{p}_2}z}$		$\varphi_{\mathrm{dc}}=2I_{\mathrm{dc}}^2$
$\varphi_{\mathrm{p}_{12}}$	$A_{0,\mathrm{p}_1}A_{0,\mathrm{p}_2}^*\mathrm{e}^{-(\alpha_{\mathrm{p}_1}+\alpha_{\mathrm{p}_2})z}$		$\varphi_{\mathrm{p},dc}=2I_{\mathrm{dc}}A_{0,\mathrm{p}}\mathrm{e}^{-\alpha_{\mathrm{p}}z}$
$\eta_{\mathrm{p}_{11}}$	1	0	1
$\eta_{\mathrm{p}_{22}}$	1	1	1/2
κ_{s}	$\varphi_s'\mathrm{e}^{(\alpha_{\mathrm{s}}-\alpha_{\mathrm{i}})z}$	$\varphi_s'\mathrm{e}^{(\alpha_{\mathrm{s}}-\alpha_{\mathrm{i}})z}$	$\varphi_s'\mathrm{e}^{(\alpha_{\mathrm{s}}-\alpha_{\mathrm{i}})z}$
κ_{i}	$\varphi_i'\mathrm{e}^{(-\alpha_{\mathrm{s}}+\alpha_{\mathrm{i}})z}$	$\varphi_i'\mathrm{e}^{(-\alpha_{\mathrm{s}}+\alpha_{\mathrm{i}})z}$	$\varphi_i'\mathrm{e}^{(-\alpha_{\mathrm{s}}+\alpha_{\mathrm{i}})z}$
φ_{s}'	$-i\frac{\beta_{\mathrm{nl}}\beta_{\mathrm{s}}^2}{4I_*^2\gamma_{\mathrm{s}}}\varphi_{\mathrm{p}_{12}}$	$\frac{\varphi_{\mathrm{s}}}{2}$	$-i\frac{\beta_{\mathrm{nl}}\beta_{\mathrm{s}}^2}{4I_*^2\gamma_{\mathrm{s}}}\varphi_{\mathrm{p},dc}$
φ_{i}'	$-i\frac{\beta_{\mathrm{nl}}\beta_{\mathrm{i}}^2}{4I_*^2\gamma_{\mathrm{i}}}\varphi_{\mathrm{p}_{12}}$	$\frac{\varphi_{\mathrm{i}}}{2}$	$-i\frac{\beta_{\mathrm{nl}}\beta_{\mathrm{i}}^2}{4I_*^2\gamma_{\mathrm{i}}}\varphi_{\mathrm{p},dc}$
φ_{s}	$-i\frac{\beta_{\mathrm{nl}}\beta_{\mathrm{s}}^2}{4I_*^2\gamma_{\mathrm{s}}}(\varphi_{\mathrm{p}_{11}}+\varphi_{\mathrm{p}_{22}})$	$-i\frac{\beta_{\mathrm{nl}}\beta_{\mathrm{s}}^2}{4I_*^2\gamma_{\mathrm{s}}}(2\varphi_{pp})$	$-i\frac{\beta_{\mathrm{nl}}\beta_{\mathrm{s}}^2}{4I_*^2\gamma_{\mathrm{s}}}(\varphi_{pp}+\varphi_{\mathrm{dc}})$
φ_{i}	$-i\frac{\beta_{\mathrm{nl}}\beta_{\mathrm{i}}^2}{4I_*^2\gamma_{\mathrm{i}}}(\varphi_{\mathrm{p}_{11}}+\varphi_{\mathrm{p}_{22}})$	$-i\frac{\beta_{\mathrm{nl}}\beta_{\mathrm{i}}^2}{4I_*^2\gamma_{\mathrm{i}}}(2\varphi_{pp})$	$-i\frac{\beta_{\mathrm{nl}}\beta_{\mathrm{i}}^2}{4I_*^2\gamma_{\mathrm{i}}}(\varphi_{pp}+\varphi_{\mathrm{dc}})$
Δ_ϕ	$\Delta_\beta+\Delta_\varphi$	$\Delta_\beta+\Delta_\varphi$	$\Delta_\beta+\Delta_\varphi$
Δ_β	$\beta_{\mathrm{p}_1}+\beta_{\mathrm{p}_2}-\beta_{\mathrm{s}}-\beta_{\mathrm{i}}$	$2\beta_{\mathrm{p}}-\beta_{\mathrm{s}}-\beta_{\mathrm{i}}$	$\beta_{\mathrm{p}}-\beta_{\mathrm{s}}-\beta_{\mathrm{i}}$
Δ_φ	$\varphi_{\mathrm{p}_1}+\varphi_{\mathrm{p}_2}-\varphi_{\mathrm{s}}-\varphi_{\mathrm{i}}$	$2\varphi_{\mathrm{p}}-\varphi_{\mathrm{s}}-\varphi_{\mathrm{i}}$	$\varphi_{\mathrm{p}}-\varphi_{\mathrm{s}}-\varphi_{\mathrm{i}}$
Δ_α	$\alpha_{\mathrm{p}_1}+\alpha_{\mathrm{p}_2}+\alpha_{\mathrm{s}}+\alpha_{\mathrm{i}}$	$2\alpha_{\mathrm{p}}+\alpha_{\mathrm{s}}+\alpha_{\mathrm{i}}$	$\alpha_{\mathrm{p}}+\alpha_{\mathrm{s}}+\alpha_{\mathrm{i}}$

Appendix D. stopband, wavevector and ripples considerations

Stopbands.——A main advantage of the framework introduced in this manuscript is that it only relies on the dispersion (or wavevector) data from the TWPA design to predict the gain behaviour. Several techniques can be used to obtain the dispersion data, such as 2D/3D EM simulators, circuit-model software, analytical expressions or measured data. Often, in the design process, computer-based simulations are employed to predict this dispersion relation of the TWPA, particularly to engineer their characteristics by introducing dispersion-engineered elements to create stopband gaps, either with periodic loading [23] or resonance-phased matching [22] techniques. These techniques allow to satisfy the phase-matching condition and achieve exponential gain. In this case, near the edges of the stopbands the wavevector will diverge exponentially away from the otherwise linear relation, approaching $\pm\infty$ at the centre of the gap. The pump tone is then placed near these edges to provide the additional phase correction required. Within the stopband itself, as the wavevector tends to infinity, all the propagating tones will become evanescent, hence no gain is expected in this region as demonstrated in many experiments [19, 22, 23]. However, this effect is difficult to calculate numerically due to the 'cumulative' nature of the wavevector relation i.e. the need to unfold the calculated data that is generally given within the $\pm180°$ range. Most often, the simulated data in this region is given as not-a-number or very small values (tend to zero instead of infinity), resulting in a 'flat' response in the cumulative curve instead of a large divergence.

For producing the curves presented in figures 3(b) and (c), we use the analytical expressions presented in [23] to generate the ABCD matrix of a unit cell, that is further cascaded to simulate the entire TWPA transmission line. We then extract the wavevector from the phase of the resulting S_{21} profile. As shown in figure 6(a), the calculated S_{21} clearly depicts the numerical artefact described above within the stopband, resulting in a finite wavevector instead of values approaching infinity. Hence, the artificial gain values inside the stopband as shown in figure 6(b). If we replace the numerical artefact within the gap with the 'corrected data' to emulate a more realistic divergence wavevector (orange dots in figure 6(a)), as expected, there is no gain observed in this area (dashed orange curve in figure 6(b)). As the behaviour of the TWPA inside the stopband is largely undefined even with measured data, and has negligible effect on the gain profile, we opt not to present this 'corrected' gain curve with an 'artificially altered' wavevector. Instead, the original curve provided by our simulation software (even it contains a numerical artefact) is used when producing the results in figure 3, to reflect the authenticity of our methodology.

Wavevector.——As observed in [23], the gap position in a JTWPA with periodic loading, such as the modulated-array design, shifts with pump power. Since the wavevector is defined as $\beta_m=\omega_m\sqrt{L_0C_{\mathrm{s}}}=\omega_{\mathrm{m}}/v_{0,\,\mathrm{unpumped}}$ in our generalised CMEs (equation (16)), where $v_{0,\,\mathrm{unpumped}}=1/\sqrt{L_0C_{\mathrm{s}}}$ is the unpumped phase velocity, extracting γ_m from the S_{21} requires correcting β_m to preserve $v_{0,\,\mathrm{unpumped}}$ while accounting for the stopband shift.

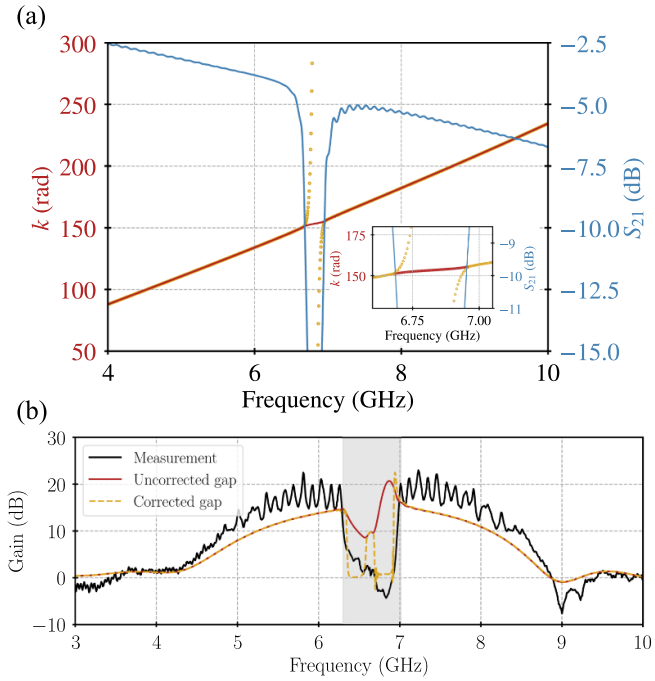

Figure 6. (a) Wavevector (red) and transmission (blue) for the entire JTWPA used to calculate the gain curve in figure 3(c). We can notice the well-defined values of the wavevector inside the bandgap originated from numerical artefacts. The orange dots represent a more realistic correction of the wavevector inside the bandgap, where it diverges exponentially approaching a singularity. (b) Measured data (black) compared with the theoretical curve presented in figure 3(c) (red) and the gain curve calculated using the dispersion curve 'artificially corrected' inside the bandgap (orange). The zero-gain gap region matches closely to the measured data.

To do this, we compute the device's S-parameters in both pumped and unpumped conditions using circuit theory and cascading `ABCD` matrices, as explained before. The inductance with applied pump is derived from equation (2). This yields the transmission and wavevector shown in figures 7(a) and (b). We extract v_0 in both cases via linear fit to the low-frequency region (below the gap), and compute the ratio $\delta = v_{0,\text{unpumped}}/v_{0,\text{pumped}}$. The corrected wavevector is then $\beta_{m,\text{corr}} = \delta\beta_{m,\text{pumped}}$, maintaining the unpumped v_0 while incorporating the stopband shift as required in the CMEs (see dotted red line in figure 7(b)).

Gain ripples.——All the TWPA implementations to date have measured gain ripples in the gain profile. Numerous factors contribute to this effect e.g. the reflections from bondwires connecting the chip, unexpected impedance mismatches with the 50 Ω environment when the device is pumped, etc. This gain ripple effect can be modelled independently from our framework by considering a Fabry-Pérot cavity model of the device as introduced in [23], using the following expression for the signal transmitted through the device (t_{tot}):

$$|t_{\text{tot}}|^2 = \frac{t^4|\Lambda|^2}{1 + r^4|\Lambda|^2 - 2r^2|\Lambda|\cos\left(2\beta_s N_{\text{jj}} + \arg\Lambda\right)} \tag{D1}$$

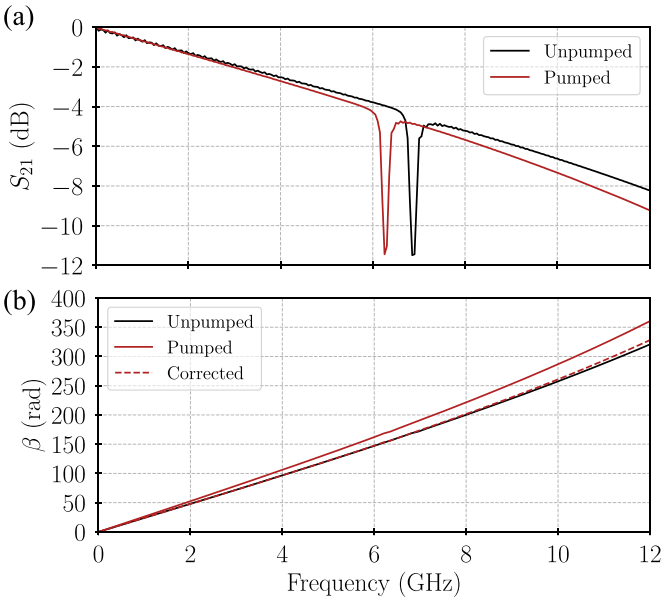

Figure 7. (a) Simulated S_{21} for the modulated-array JTWPA in [23] under pumped (red) and unpumped (black) conditions, showing the shift of the stopband with applied pump power. Note that the higher losses at high frequencies for the pumped case result from a larger electrical length of the device due to the change in v_0. (b) Corresponding wavevector β_m, extracted from the phase of the S_{21}. The corrected wavevector $\beta_{m,\text{corr}}$ (dotted red line) is obtained by rescaling the pumped wavevector to maintain the unpumped v_0 while preserving the pump-induced stopband shift, as required in the CME formalism.

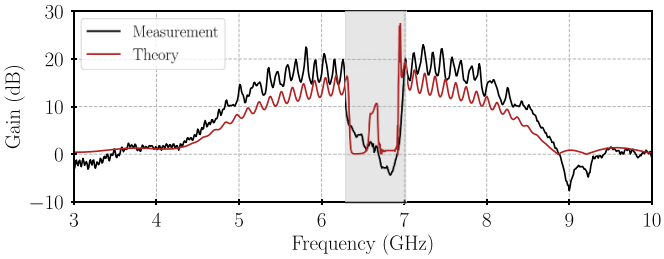

Figure 8. Measured data (black) and theoretical curve (red) as presented in figure 3(c), including the Fabry–Pérot cavity effect with a reflection coefficient of $r = 0.1$ resulting in gain ripples.

where r and t are the reflection and transmission coefficients respectively, Λ is the transmitted signal without considering reflections and N_{jj} is the number of junctions in the JTWPA (in this expression β_s is defined as radians per junction). Applying this expression to the theoretical curve presented in figure 6(b) with the 'corrected gap', using $r = 0.1$ and $t = 0.995$, we obtain the result presented in figure 8. Nevertheless, due to the lack of certainties in estimating r and t in the experimental data presented in this manuscript, gain ripples are not included in our calculations in figure 3.

ORCID iDs

Javier Navarro Montilla https://orcid.org/0000-0003-4423-8400
Boon-Kok Tan https://orcid.org/0000-0002-6252-9351

References

[1] Castellanos-Beltran M A, Irwin K D, Vale L R, Hilton G C and Lehnert K W 2009 Bandwidth and dynamic range of a widely tunable josephson parametric amplifier *IEEE Trans. Appl. Supercond.* **19** 944–7

[2] Zhong L *et al* 2013 Squeezing with a flux-driven josephson parametric amplifier *New J. Phys.* **15** 125013

[3] Zhou X, Schmitt V, Bertet P, Vion D, Wustmann W, Shumeiko V and Estève D 2014 High-gain weakly nonlinear flux-modulated josephson parametric amplifier using a squid array *Phys. Rev. B* **89** 214517

[4] Eichler C and Wallraff A 2014 Controlling the dynamic range of a josephson parametric amplifier *EPJ Quantum Technol.* **1** 2

[5] Burnett J J, Bengtsson A, Scigliuzzo M, Niepce D, Kudra M, Delsing P and Bylander J 2019 Decoherence benchmarking of superconducting qubits *npj Quantum Inf.* **5** 1–8

[6] Lin Z, Inomata K, Oliver W, Koshino K, Nakamura Y, Tsai J S and Yamamoto T 2013 Single-shot readout of a superconducting flux qubit with a flux-driven josephson parametric amplifier *Appl. Phys. Lett.* **103** 132602

[7] Krantz P, Bengtsson A, Simoen M, Gustavsson S, Shumeiko V, Oliver W, Wilson C, Delsing P and Bylander J 2016 Single-shot read-out of a superconducting qubit using a josephson parametric oscillator *Nat. Commun.* **7** 11417

[8] Besse J-C, Gasparinetti S, Collodo M C, Walter T, Kurpiers P, Pechal M, Eichler C and Wallraff A 2018 Single-shot quantum nondemolition detection of individual itinerant microwave photons *Phys. Rev. X* **8** 021003

[9] Kundu S, Gheeraert N, Hazra S, Roy T, Salunkhe K V, Patankar M P and Vijay R 2019 Multiplexed readout of four qubits in 3D cQED architecture using broadband JPA *Appl. Phys. Lett.* **114** 172601

[10] Malnou M, Palken D, Brubaker B, Vale L R, Hilton G C and Lehnert K 2019 Squeezed vacuum used to accelerate the search for a weak classical signal *Phys. Rev. X* **9** 021023

[11] Shokair T *et al* 2014 Future directions in the microwave cavity search for dark matter axions *Int. J. Mod. Phys.* A **29** 1443004

[12] Malnou M, Palken D, Vale L R, Hilton G C and Lehnert K 2018 Optimal operation of a josephson parametric amplifier for vacuum squeezing *Phys. Rev. Appl.* **9** 044023

[13] Zhong L *et al* 2018 Results from phase 1 of the haystac microwave cavity axion experiment *Phys. Rev. D* **97** 092001

[14] van Bibber K, Lehnert K and Chou A 2019 Putting the squeeze on axions *Phys. Today* **72** 48–55

[15] Cullen A 1958 A travelling-wave parametric amplifier *Nature* **181** 332

[16] Tien P 1958 Parametric amplification and frequency mixing in propagating circuits *J. Appl. Phys.* **29** 1347–57

[17] Louisell W, Yariv A and Siegman A 1961 Quantum fluctuations and noise in parametric processes. I *Phys. Rev.* **124** 1646

[18] Caves C M, Combes J, Jiang Z and Pandey S 2012 Quantum limits on phase-preserving linear amplifiers *Phys. Rev. A* **86** 063802

[19] Eom B H, Day P K, LeDuc H G and Zmuidzinas J 2012 A wideband, low-noise superconducting amplifier with high dynamic range *Nat. Phys.* **8** 623

[20] Sweeny M and Mahler R 1985 A travelling-wave parametric amplifier utilizing josephson junctions *IEEE Trans. Magn.* **21** 654–5

[21] Yurke B, Roukes M, Movshovich R and Pargellis A 1996 A low-noise series-array josephson junction parametric amplifier *Appl. Phys. Lett.* **69** 3078–80

[22] Macklin C, O'Brien K, Hover D, Schwartz M, Bolkhovsky V, Zhang X, Oliver W and Siddiqi I 2015 A near–quantum-limited josephson traveling-wave parametric amplifier *Science* **350** 307–10

[23] Planat L, Ranadive A, Dassonneville R, Martinez J P, Leger S, Naud C, Buisson O, Hasch-Guichard W, Basko D M and Roch N 2020 Photonic-crystal josephson traveling-wave parametric amplifier *Phys. Rev. X* **10** 021021

[24] Zorin A 2019 Flux-driven josephson traveling-wave parametric amplifier *Phys. Rev. Appl.* **12** 044051

[25] White T *et al* 2015 Traveling wave parametric amplifier with josephson junctions using minimal resonator phase matching *Appl. Phys. Lett.* **106** 242601

[26] Adamyan A, De Graaf S, Kubatkin S and Danilov A 2016 Superconducting microwave parametric amplifier based on a quasi-fractal slow propagation line *J. Appl. Phys.* **119** 083901

[27] Vissers M R, Erickson R P, Ku H-S, Vale L, Wu X, Hilton G and Pappas D P 2016 Low-noise kinetic inductance traveling-wave amplifier using three-wave mixing *Appl. Phys. Lett.* **108** 012601

[28] Chaudhuri S, Li D, Irwin K, Bockstiegel C, Hubmayr J, Ullom J, Vissers M and Gao J 2017 Broadband parametric amplifiers based on nonlinear kinetic inductance artificial transmission lines *Appl. Phys. Lett.* **110** 152601

[29] Miano A and Mukhanov O A 2019 Symmetric traveling wave parametric amplifier *IEEE Trans. Appl. Supercond.* **29** 1–6

[30] Bell M and Samolov A 2015 Traveling-wave parametric amplifier based on a chain of coupled asymmetric squids *Phys. Rev. Appl.* **4** 024014

[31] Yaakobi O, Friedland L, Macklin C and Siddiqi I 2013 Parametric amplification in josephson junction embedded transmission lines *Phys. Rev. B* **87** 144301

[32] O'Brien K, Macklin C, Siddiqi I and Zhang X 2014 Resonant phase matching of josephson junction traveling wave parametric amplifiers *Phys. Rev. Lett.* **113** 157001

[33] van der Reep T 2019 Mesoscopic hamiltonian for josephson traveling-wave parametric amplifiers *Phys. Rev. A* **99** 063838

[34] Chaudhuri S, Gao J and Irwin K 2014 Simulation and analysis of superconducting traveling-wave parametric amplifiers *IEEE Trans. Appl. Supercond.* **25** 1–5

[35] Erickson R P and Pappas D P 2017 Theory of multiwave mixing within the superconducting kinetic-inductance traveling-wave amplifier *Phys. Rev. B* **95** 104506

[36] Zhao S, Withington S, Goldie D J and Thomas C N 2019 Loss and saturation in superconducting travelling-wave parametric amplifiers *J. Phys. D: Appl. Phys.* **52** 415301

[37] Dixon T, Dunstan J W, Long G B, Williams J M, Meeson P J and Shelly C D 2020 Capturing complex behaviour in josephson travelling wave parametric amplifiers *Phys. Rev. Applied* **14** 034058

[38] Bockstiegel C, Gao J, Vissers M, Sandberg M, Chaudhuri S, Sanders A, Vale L, Irwin K and Pappas D 2014 Development of a broadband nbtin traveling wave parametric amplifier for mkid readout *J. Low Temp. Phys.* **176** 476–82

[39] Shan W, Sekimoto Y and Noguchi T 2016 Parametric amplification in a superconducting microstrip transmission line *IEEE Trans. Appl. Supercond.* **26** 1–9

[40] Pozar D 2011 *Microwave Engineering* 4th edn (Wiley)

[41] Bardeen J 1962 Critical fields and currents in superconductors *Rev. Mod. Phys.* **34** 667–81

[42] Kalacheva D, Fedorov G, Khrapach I and Astafiev O 2023 Coplanar superconducting resonators with nonlinear kinetic inductance bridge *Supercond. Sci. Technol.* **36** 055011

[43] Swenson L J, Day P K, Eom B H, Leduc H G, Llombart N, McKenney C M, Noroozian O and Zmuidzinas J 2013 Operation of a titanium nitride superconducting

microresonator detector in the nonlinear regime *J. Appl. Phys.* **113** 104501
[44] Clem J R and Kogan V G 2012 Kinetic impedance and depairing in thin and narrow superconducting films *Phys. Rev.* B **86** 174521
[45] Kubo T 2020 Superfluid flow in disordered superconductors with dynes pair-breaking scattering: depairing current, kinetic inductance and superheating field *Phys. Rev. Res.* **2** 033203
[46] Kubo T 2024 Erratum: superfluid flow in disordered superconductors with dynes pair-breaking scattering: depairing current, kinetic inductance and superheating field [Phys. Rev. Res. 2 033203 (2020)] *Phys. Rev. Res.* **6** 039002
[47] Kubo T 2024 Significant contributions of the higgs mode and impurity-scattering self-energy corrections to the low-frequency complex conductivity in dc-biased superconducting devices *Phys. Rev. Appl.* **22** 044042
[48] Planat L 2020 Resonant and traveling-wave parametric amplification near the quantum limit Resonant and traveling-wave parametric amplification near the quantum limit University of Grenoble Alpes
[49] Tan B, Boussaha F, Chaumont C, Longden J and Montilla J N 2022 Engineering the thin film characteristics for optimal performance of superconducting kinetic inductance amplifiers using a rigorous modelling technique *Open Research Europe* vol 2
[50] Stolen R and Bjorkholm J 1982 Parametric amplification and frequency conversion in optical fibers *IEEE J. Quantum Electron.* **18** 1062–72
[51] Ansys hfss (available at: www.ansys.com/products/electronics/ansys-hfss)
[52] Sonnet software (available at: www.sonnetsoftware.com/)
[53] Sweetnam T, Banys D, Gilles V, McCulloch M A and Piccirillo L 2022 Simulating the behaviour of travelling wave superconducting parametric amplifiers using a commercial circuit simulator *Supercond. Sci. Technol.* **35** 095011
[54] Mattis D C and Bardeen J 1958 Theory of the anomalous skin effect in normal and superconducting metals *Phys. Rev.* **111** 412–7
[55] Gurevich A 2014 Reduction of dissipative nonlinear conductivity of supercon- ductors by static and microwave magnetic fields *Phys. Rev. Lett.* **113** 087001
[56] Kubo T and Gurevich A 2019 Field-dependent nonlinear surface resistance and its optimization by surface nanostructuring in superconductors *Phys. Rev. B* **100** 064522
[57] Zhao S, Goldie D J, Thomas C N and Withington S 2018 Calculation and measurement of critical temperature in thin superconducting multilayers *Supercond. Sci. Technol.* **31** 105004
[58] Kher A, Day P K, Eom B H, Zmuidzinas J and Leduc H G 2016 Kinetic inductance parametric up-converter *J. Low Temp. Phys.* **184** 480–5
[59] Tan B-K, Klimovich N, Stephenson R, Faramarzi F and Day P 2024 Operation of kinetic-inductance travelling wave parametric amplifiers at millimetre wavelengths *Supercond. Sci. Technol.* **37** 035006
[60] Shu S, Klimovich N, Eom B H, Beyer A, Thakur R B, Leduc H and Day P 2021 Nonlinearity and wide-band parametric amplification in a (Nb,Ti)N n microstrip transmission line *Phys. Rev. Res.* **3** 023184
[61] Ratter K and Tan B-K 2021 *A dispersion-engineered Josephson Travelling wave Parametric Amplifier with Periodic Impedance Perturbation* (NationalRadio Astronomy Observatory)
[62] Gaydamachenko V, Kissling C and Grünhaupt L 2025 An RF-squid-based traveling-wave parametric amplifier with -84 DBM input saturation power across more than one octave bandwidth
[63] Roudsari A F *et al* 2023 Three-wave mixing traveling-wave parametric amplifier with periodic variation of the circuit parameters *Appl. Phys. Lett.* **122** 052601
[64] Reyes-Ayona J R and Halevi P 2015 Observation of genuine wave vector (k or β) gap in a dynamic transmission line and temporal photonic crystals *Appl. Phys. Lett.* **107** 074101
[65] Khalil M S *et al* 2013 Evidence for hydrogen two-level systems in atomic layer deposition oxides *Appl. Phys. Lett.* **103** 162601